

# Tunable Inductive Coupler for High-Fidelity Gates Between Fluxonium Qubits

Helin Zhang,<sup>1,2,†,§</sup> Chunyang Ding<sup>¶</sup>,<sup>1,2,3,§</sup> D.K. Weiss<sup>¶</sup>,<sup>4,5</sup> Ziwen Huang<sup>¶</sup>,<sup>4,‡</sup> Yuwei Ma,<sup>6,7</sup> Charles Guinn,<sup>8</sup> Sara Sussman,<sup>8</sup> Sai Pavan Chitta<sup>¶</sup>,<sup>4</sup> Danyang Chen<sup>¶</sup>,<sup>4</sup> Andrew A. Houck,<sup>8</sup> Jens Koch<sup>¶</sup>,<sup>4</sup> and David I. Schuster<sup>1,2,3,9,\*</sup>

<sup>1</sup>*James Franck Institute, University of Chicago, Chicago, Illinois 60637, USA*

<sup>2</sup>*Department of Physics, University of Chicago, Chicago, Illinois 60637, USA*

<sup>3</sup>*Department of Physics and Applied Physics, Stanford University, Stanford, California 94305, USA*

<sup>4</sup>*Department of Physics and Astronomy, Northwestern University, Evanston, Illinois 60208, USA*

<sup>5</sup>*Yale Quantum Institute, Yale University, New Haven, Connecticut 06511, USA*

<sup>6</sup>*Hefei National Research Center for Physical Sciences at the Microscale and School of Physical Sciences, University of Science and Technology of China, Hefei 230026, China*

<sup>7</sup>*Shanghai Research Center for Quantum Science and CAS Center for Excellence in Quantum Information and Quantum Physics, University of Science and Technology of China, Shanghai 201315, China*

<sup>8</sup>*Department of Physics, Princeton University, Princeton, New Jersey 08544, USA*

<sup>9</sup>*Pritzker School of Molecular Engineering, University of Chicago, Chicago, Illinois 60637, USA*



(Received 18 September 2023; accepted 14 March 2024; published 2 May 2024)

The fluxonium qubit is a promising candidate for quantum computation due to its long coherence times and large anharmonicity. We present a tunable coupler that realizes strong inductive coupling between two heavy-fluxonium qubits, each with approximately 50-MHz frequencies and approximately 5-GHz anharmonicities. The coupler enables the qubits to have a large tuning range of  $XX$  coupling strengths ( $-35$  to  $75$  MHz). The  $ZZ$  coupling strength is  $<3$  kHz across the entire coupler bias range and  $<100$  Hz at the coupler off position. These qualities lead to fast high-fidelity single- and two-qubit gates. By driving at the difference frequency of the two qubits, we realize a  $\sqrt{iSWAP}$  gate in 258 ns with fidelity 99.72%, and by driving at the sum frequency of the two qubits, we achieve a  $\sqrt{bSWAP}$  gate in 102 ns with fidelity 99.91%. This latter gate is only five qubit Larmor periods in length. We run cross-entropy benchmarking for over 20 consecutive hours and measure stable gate fidelities, with  $\sqrt{bSWAP}$  drift ( $2\sigma$ )  $<0.02\%$  and  $\sqrt{iSWAP}$  drift  $<0.08\%$ .

DOI: [10.1103/PRXQuantum.5.020326](https://doi.org/10.1103/PRXQuantum.5.020326)

## I. INTRODUCTION

Superconducting circuits are a promising platform for the development of scalable error-corrected quantum computation, heralded by many recent advances toward

large-scale quantum processors [1,2] and improvements on the performance of qubits and gate operations [3–5]. These advances have relied on the transmon qubit [6] and, through collective effort, these qubits have achieved excellent coherence times [5,7] and gate fidelities approaching the quantum error-correction threshold [8–10].

A promising alternative to the transmon is the fluxonium qubit [11], which has attractive properties including a nearly degenerate ground state and a large anharmonicity. Compared to other qubits fabricated with similar material qualities, low-frequency qubits have less dielectric loss and thus a slower decoherence rate. The large anharmonicity mitigates the speed limit for qubit operations in transmons and enables quantum gates that are as fast or even faster despite low qubit frequencies [12]. In addition, one can flux tune the fluxonium qubit to be noise biased, increasing energy coherence ( $T_1 > 5$  ms) at the expense of being more phase sensitive [13,14]. Recent works have demonstrated approximately 1 ms coherence times and

\*Corresponding author: dschus@stanford.edu

†Current address: Research Laboratory of Electronics, Massachusetts Institute of Technology, Cambridge, Massachusetts 02139, USA.

‡Current address: Superconducting Quantum Materials and Systems Center, Fermi National Accelerator Laboratory (FNAL), Batavia, Illinois 60510, USA.

§These authors contributed equally to this work.

Published by the American Physical Society under the terms of the [Creative Commons Attribution 4.0 International license](#). Further distribution of this work must maintain attribution to the author(s) and the published article's title, journal citation, and DOI.

>99.9% fidelity single-qubit gates using fluxonium qubits [15–17]. In addition, one can flux tune the fluxonium qubit to be noise biased, increasing energy coherence ( $T_1 > 5$  ms) at the expense of being more phase sensitive [13,14].

Beyond single-qubit operations, several recent works have demonstrated high-fidelity two-qubit fluxonium gates using either fixed capacitive coupling [18–21] or a tunable capacitive coupler [17,22]. While these two-qubit gate schemes are promising, they either populate states outside of the computational subspace or use high-frequency fluxonium qubits. In this work, we realize a tunable *inductive* coupler and perform (>99.9%) fidelity two-qubit gates. Our inductive coupler, similar to the g-mon coupler [23,24], realizes a large interaction strength even for low-frequency qubits, without involving higher energy levels. This enables the gate to take advantage of the full coherence of the fluxonium while avoiding any leakage to states outside the logical subspace.

In Sec. II, we provide theoretical analysis of our tunable inductive coupler, showing the origins of  $XX$  coupling. We also find that both the  $XX$  and unwanted  $ZZ$  coupling can be turned off, allowing for an operational spot for single-qubit gates. In Sec. III, we report the

characterization of our device near this operational spot, measuring the  $ZZ$  coupling to be <100 Hz. Finally, in Sec. IV, we construct  $\sqrt{i}\text{SWAP}$  and  $\sqrt{b}\text{SWAP}$  gates using this  $XX$  interaction. We demonstrate the tuning of these gates and estimate their fidelities using various benchmarking protocols.

## II. INDUCTIVELY COUPLED HEAVY-FLUXONIUM QUBITS

In this paper, we use a tunable inductive coupler, inspired by designs from Refs. [23–26], to realize strong coupling between two fluxonium qubits. Each qubit is individually described by the Hamiltonian

$$H_f = -4E_C \frac{d^2}{d\varphi^2} - E_J \cos(\varphi) + \frac{1}{2}E_L \left( \varphi + 2\pi \frac{\Phi_{\text{ext}}}{\Phi_0} \right)^2, \quad (1)$$

where  $E_C = e^2/(2C_q)$  denotes the charging energy,  $C_q$  is the total shunting capacitance of the qubit,  $E_J$  is the Josephson energy of the small junction,  $E_L = \Phi_0^2/(4\pi^2 L_{JA})$  is the inductive energy, and  $L_{JA}$  is the total

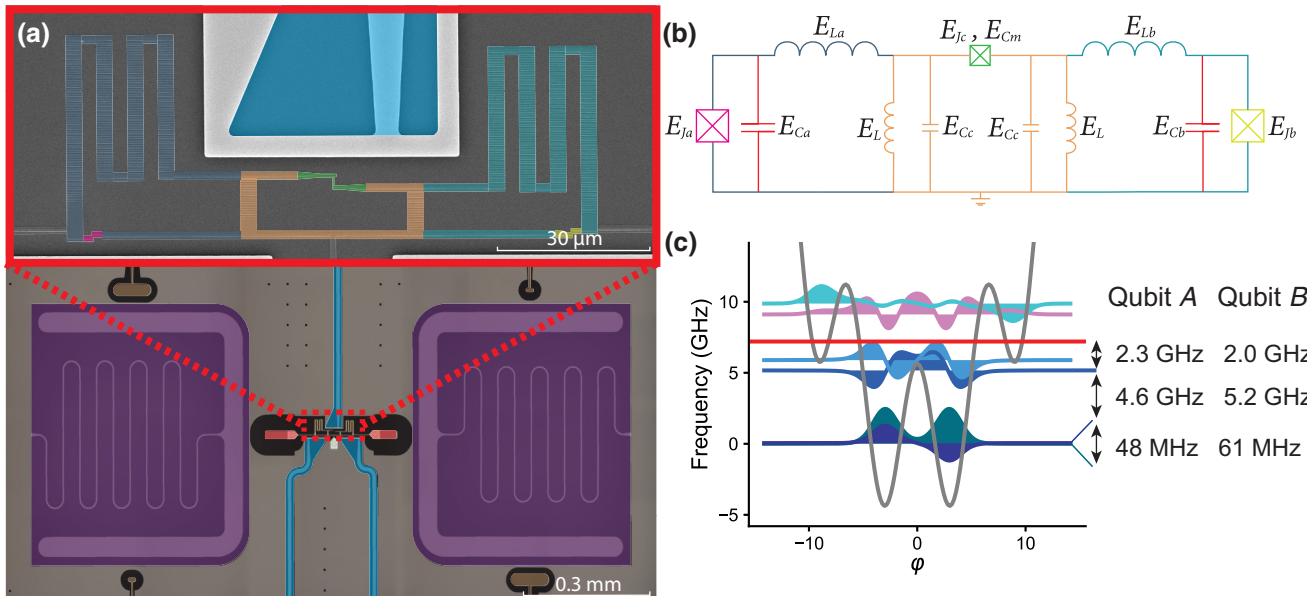


FIG. 1. The device, circuit, and energy-level diagram. (a) Top panel: False-colored scanning electron microscope image of the two fluxoniums and coupler junction loops. Each qubit consists of a small Josephson junction (pink and yellow) and an array of large junctions as an inductor (blue and cyan). The coupler consists of a small Josephson junction (green) and a shorter array of junctions (orange). Bottom panel: optical microscope image of the flux control lines (light blue), readout resonators (purple), qubit shunting capacitors (red), and resonator drive and readout lines (brown). (b) Circuit diagram for the coupled fluxoniums with the tunable coupler. The colors of the components correspond to the colors in the device images. (c) Energy-level diagram of the heavy-fluxonium wave functions at the flux-frustration point ( $\Phi_{\text{ext}} = \Phi_0/2$ ), plotted using qubit-B parameters. The gray line represents the potential well, and the red line is at the readout resonator frequency. The first six energy eigenstate wave functions are plotted with solid colors. The qubit frequencies, anharmonicities, and resonator detunings for qubits A and B are indicated with black arrows.

inductance of the superinductor.  $\Phi_0 = h/2e$  is the superconducting flux quantum and  $\Phi_{\text{ext}}$  denotes the flux threading the loop. We design heavy-fluxonium qubits [Fig. 1(a)] with large  $E_J/E_C$ , such that at half-integer flux bias, our qubits, labeled as  $A$  and  $B$ , have small splittings ( $\omega_A/2\pi = 48$  MHz and  $\omega_B/2\pi = 61$  MHz) and large anharmonicities ( $\alpha_A = 4.6$  GHz and  $\alpha_B = 5.2$  GHz). See Fig. 1(c) for the qubit-level structure at the sweet spot ( $\Phi_{\text{ext}} = \Phi_0/2$ ) and Table I for the qubit parameters.

These two heavy-fluxonium qubits are linked via an inductive coupler, as shown in Fig. 1(b). This full circuit, analyzed in Appendix A, consists of four degrees of freedom: the two fluxonium qubits and the two coupler degrees of freedom—one harmonic and one fluxoniumlike. Ignoring the negligible cross capacitance, these two fluxonium qubits do not directly interact with each other; instead, they each share an inductance ( $E_L$ ) with the tunable coupler. Although the galvanic coupling is relatively strong, the coupler excitation energies (9.5 GHz) are well above the energies associated with qubit excitations, leading to a dispersive interaction. Thus, near half-integer flux for the qubits, we can use a perturbative treatment, creating an effective Hamiltonian up to fourth order [27]:

$$H_{\text{eff}} = \sum_{\mu=A,B} \left( -\frac{\omega_\mu}{2} \sigma_z^\mu - \Omega_\mu \sigma_x^\mu \right) + J \sigma_x^A \sigma_x^B + \zeta \sigma_z^A \sigma_z^B, \quad (2)$$

where  $\sigma_x^\mu$  and  $\sigma_z^\mu$  are the qubit Pauli operators in the basis of symmetric and antisymmetric wave functions.

The first term in the effective Hamiltonian describes the qubit frequencies, including the Lamb shifts induced by the coupler. The second term captures the effect of qubit flux bias, which we use for single-qubit gates [12]. This term additionally incorporates a first-order perturbative

TABLE I. The parameters and basic properties for the qubits. Measurements are made when the fluxonium qubits are biased at their half-flux sweet spots, while the coupler  $\varphi_-$  mode is biased at  $\Phi_{\text{ext},C}/\Phi_0 = 0.3$ . The energy splittings are the differences between the bare-ground- and first-excited-state energies  $f_{10} = f_1 - f_0$ , while the anharmonicity is defined as  $\alpha = f_{21} - f_{10}$ . Circuit parameters in gigahertz are used throughout this work.  $T_2$  in this table refers to the values when the other qubit is at its ground state.

	Qubit $A$	Qubit $B$	Coupler $\varphi_-$	Coupler $\varphi_+$
$f_{10}$ (GHz)	0.0484	0.0618	9.52	15.6
$\alpha$ (GHz)	5.06	4.41	0.93	0
$T_1$ ( $\mu$ s)	300	180		
$T_2^*$ ( $\mu$ s)	200	150		
$T_{2e}$ ( $\mu$ s)	300	250		
$E_J$ (GHz)	4.88	5.65	4.246	
$E_C$ (GHz)	0.905	0.95	8	12
$E_L$ (GHz)	0.286	0.292	3.52	3.52

shift due to the fluxoniumlike coupler degree of freedom. The third term is the desired  $XX$  coupling, where  $J$  is a function of the coupler flux  $\Phi_{\text{ext},C}$ . Virtual exchanges through coupler excitations leads to a  $\varphi_A \varphi_B$  term, which can be truncated to  $\sigma_x^A \sigma_x^B$ . There are two contributions here: a static one, due to the harmonic coupler degree of freedom, and a flux-tunable one, from the fluxoniumlike coupler degree of freedom (see Ref. [27]). Because these contributions have opposite signs, we can null  $J$  at a particular  $\Phi_{\text{ext},C}$ , which we term the “off position.” The final term describes a small unwanted  $ZZ$  interaction that comes from fourth-order perturbation theory.

This effective Hamiltonian governs our operation of the two-qubit device: a parametric drive controls  $J$ , allowing us to achieve two-qubit gates, and a particular  $\Phi_{\text{ext},C}$  bias fully turns off the qubit-qubit coupling. However, since  $\Omega_\mu$  is coupler-flux dependent, this tuning causes shifts of the fluxonium qubits away from their sweet spots. The qubit fluxes must then be tuned to compensate for these shifts. Thus, while constraining the qubits to remain at their sweet-spot locations, we perform an effectively one-dimensional sweep over the coupler flux to locate the off position [27]. We refer to this sweep as the “sweet-spot contour.” Along the sweet-spot contour,  $\zeta$  is generally nonzero but numerically we find that  $\zeta < 3$  kHz. Effectively, this  $ZZ$  term can be cancelled via small ( $< 10^{-5} \Phi_0$ ) flux shifts away from the qubit sweet spot. We find the flux noise at this bias point not to be the dominant dephasing mechanism, as it would only limit the pure-qubit dephasing time to 1 ms (see Appendix C).

### III. DEVICE CHARACTERIZATION

We measure the properties of a fabricated two-dimensional (2D) superconducting device, validating our theoretical analysis of the tunable inductive coupler and calibrating it for single- and two-qubit gates. We use a tantalum base layer for increased qubit coherence [7,28] and we use double-angle aluminum evaporation [29] to fabricate the Josephson junctions (see Appendix F). The geometry of the device is shown in Fig. 1(a). There are 205 Josephson junctions in the superinductor of each qubit ( $E_{LA}$  and  $E_{LB}$ ) and 17 junctions in each superinductor of the tunable coupler ( $E_L$ ). There are three dedicated control lines, one for each of the qubits and one for the coupler, which are used for both dc biasing as well as rf-flux driving (see Appendix E).

There are two lumped  $LC$  resonators capacitively coupled to the fluxoniums for readout. These readout resonators have line widths of approximately 1.1 MHz and dispersive shifts of approximately 0.7 MHz from the computational levels. Since the qubit frequencies correspond to a temperature (approximately 3 mK) that is lower than the environment temperature, we must always initialize the qubit. We use a measurement-based active reset protocol

for initialization [30,31], enabled by the QICK controlled radio-frequency system on chip (RFSOC) [32]. The reset is carried out by measuring the qubit state and conditionally playing a single-qubit  $\pi$  pulse, completed within 800 ns. With this method, we initialize the qubits with approximately 95% fidelity, primarily limited by our measurement infidelity (which could be improved by using quantum noise-limited amplifiers; see Appendix G).

To determine the coupler parameters, we scan the coupler flux over the range of  $\Phi_{\text{ext},C}/\Phi_0 = 0.24$  to  $\Phi_{\text{ext},C}/\Phi_0 = 0.34$  and measure qubit frequencies while staying on the “sweet-spot contour,” shown in Fig. 2(a). Since  $\Omega_{A,B}$  is zero along this contour, we determine the  $XX$

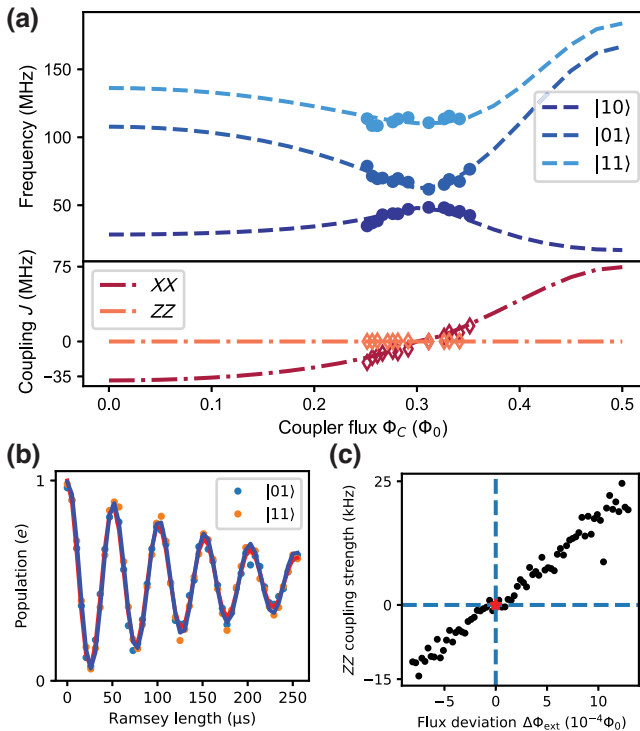


FIG. 2. Measurements of the  $XX$  and  $ZZ$  coupling strength. (a) Top panel: the measured  $|01\rangle$ ,  $|10\rangle$ , and  $|11\rangle$  frequencies as a function of the coupler flux as the qubits are tuned to be along the “sweet-spot contour.” The dashed lines are from full numerical simulations with parameters extracted from qubit spectroscopy (see Appendix A). Bottom panel: the  $XX$  and  $ZZ$  coupling strength (diamonds) extracted from the data (dots). Numerical-simulation predictions are plotted as the dashed lines. The  $ZZ$  coupling strength is  $<3$  kHz across the entire coupler flux range. (b) A Ramsey experiment with qubit  $B$  at the coupler “off position,” with the qubits initialized in either  $|01\rangle$  or  $|11\rangle$ . The frequency difference  $(f_{11} - f_{10}) - (f_{01} - f_{00})$ , extracted using Ramsey fits with different qubit initial states, measures the  $ZZ$  coupling strength to be  $<100$  Hz. (c) We perform this same measurement on qubit  $A$  while sweeping its flux away from the “sweet-spot contour.” We find that the  $ZZ$  coupling strength becomes nonzero, which we use as an indicator for fine-tuning qubit flux biases.

coupling strength  $J$  from observing the qubit frequency shifts in the dressed Hamiltonian. We measure the  $ZZ$  coupling strength by taking the difference of the frequency of qubit  $B$  when qubit  $A$  is at  $|0\rangle$  and  $|1\rangle$ . We fit the full model of the circuit to the data and find that  $J$  can be tuned to zero at  $\Phi_{\text{ext},C}/\Phi_0 \sim 0.3$ , where  $f_{01} - f_{10}$  is at its minimum. Within the range of coupler flux that we measure,  $J$  is tuned from  $-20$  MHz to  $15$  MHz. Over the whole range of coupler flux,  $\Phi_{\text{ext},C}/\Phi_0 = 0$  to  $\Phi_{\text{ext},C}/\Phi_0 = 0.5$ , numerical simulations show that  $J$  can range between  $-35$  MHz and  $70$  MHz [see Fig. 2(a)]. These coupling strengths are large, of the order of individual qubit frequencies ( $J \sim \omega_\mu$ ).

To measure the precise  $ZZ$  coupling strength, we perform Ramsey experiments on qubit  $B$ , with qubit  $A$  in its ground or excited states [see Fig. 2(b)]. We then vary the flux near the qubit sweet spots, measuring the  $ZZ$  coupling strength. As predicted by our theory, we find a  $<100$  Hz  $ZZ$  coupling-strength point at the maximum  $T_2$  point [see Fig 2(c)], implying an on-off contrast  $>10^5$ . At this coupler off position, qubit  $A$  (qubit  $B$ )  $T_1$  is  $180$   $\mu$ s ( $300$   $\mu$ s) and  $T_{2e}$  is  $250$   $\mu$ s ( $300$   $\mu$ s) (see Table I).

We bias the tunable coupler at the off position and realize both single- and two-qubit controls with rf-flux drives. Due to significant (approximately 20%) geometric dc- and rf-flux crosstalk in our system, we have off-resonant drives on both qubits. (In larger-scale chips, this level of crosstalk can be reduced by implementing a number of recent innovations [33–35].) This effectively causes dynamic qubit frequency shifts as well as unwanted  $ZX$ ,  $XZ$ , and  $ZZ$  drive terms (see Appendix D). Therefore, we develop a method to calibrate the rf-flux crosstalk by measuring its effect on qubit frequencies (see Appendix H) and apply crosstalk-cancellation pulses in our two-qubit gates.

To dynamically activate the  $XX$  coupling, we rf drive the coupler near the difference ( $f_{01} - f_{10}$ ) and sum ( $f_{01} + f_{10}$ ) frequencies of the two qubits (see Fig. 3). We sweep the frequency and length of this pulse at drive amplitudes of  $0.5\%\Phi_0$  ( $1.1\%\Phi_0$ ) and observe chevrons of correlated oscillations between  $|01\rangle$  and  $|10\rangle$  ( $|00\rangle$  and  $|11\rangle$ ), finding an oscillation rate of  $0.83$  MHz ( $2.50$  MHz). The offset from the expected frequencies is small, indicating that the crosstalk cancellation is effective.

#### IV. SINGLE- AND TWO-QUBIT GATES

We develop fast high-fidelity single- and two-qubit gates with our device. For the single-qubit gates, we flux modulate the qubits at their corresponding bare-qubit frequencies. With qubit frequencies at  $48.4$  and  $61.8$  MHz, we calibrate single-qubit  $\pi/2$  gates using Gaussian pulses with length  $83.3$  and  $65.1$  ns, which is approximately four qubit Larmor periods. We update the phases of subsequent drive pulses to implement virtual  $Z$  gates [36]. We

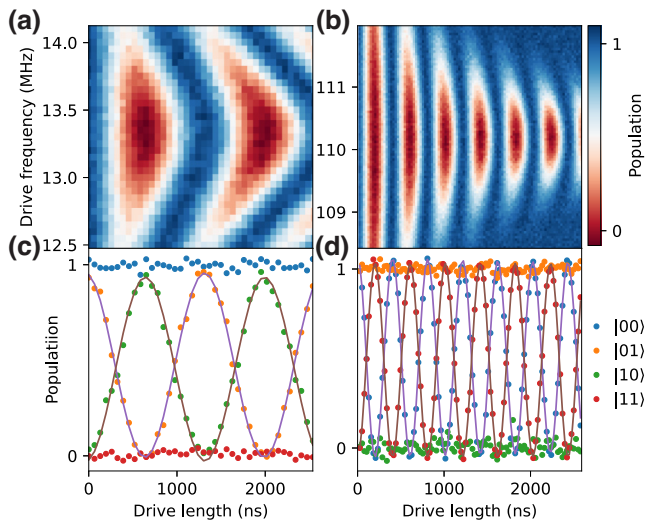


FIG. 3. The sweeping coupler drive frequencies near the difference ( $f_{01} - f_{10}$ ) and sum ( $f_{01} + f_{10}$ ) of the qubit frequencies generates chevron patterns. (a) The  $|01\rangle \leftrightarrow |10\rangle$  chevron centered at 13.3 MHz. (b) The  $|00\rangle \leftrightarrow |11\rangle$  chevron centered at 110.2 MHz. (c) After initializing the qubit to each of the four basis states, we drive the coupler at the optimal frequency and measure the population of qubit  $A$ . When driving at the difference frequency (13.3 MHz), a correlated oscillation occurs between  $|01\rangle$  and  $|10\rangle$ , where one oscillation period takes 1200 ns. The solid line indicates the best fit to the data. (d) When driving at the sum frequency (110.2 MHz), correlated oscillations occur between  $|00\rangle$  and  $|11\rangle$ , where one oscillation period takes 400 ns.

use simultaneous randomized benchmarking [37] to measure average single-qubit Clifford-gate fidelities, initially measuring qubit- $A$  (qubit- $B$ ) fidelities of 99.90% (99.88%), limited primarily by coherent errors. Thus, we further optimize the single-qubit gates using derivative removal by adiabatic gate (DRAG) shaping [38], finding that the single-qubit gate fidelities increase to 99.94% and 99.95%, respectively, for each qubit [see Fig. 4(a)].

After pulse shaping, the remaining gate infidelity is primarily from qubit decoherence. Using a master equation to simulate gate infidelities, we estimate contributions of qubit decay and dephasing to be  $4 \times 10^{-4}$  and  $3 \times 10^{-4}$ , respectively. With our current pulse length, the pulse-energy deviation from different carrier-envelope phases is not the limiting factor of our single-qubit gate fidelities. The error from such deviations is less than  $1 \times 10^{-5}$ , far lower than the dominant decoherence contribution. We also evaluate the contribution of the Bloch-Siegert shift at this drive strength to be  $5.6 \times 10^{-5}$ . The complete error analysis, including other sources of error, is performed in Appendix J.

For two-qubit gates, due to the negligibly small ZZ interaction strength and the tunable XX coupling, the intuitive

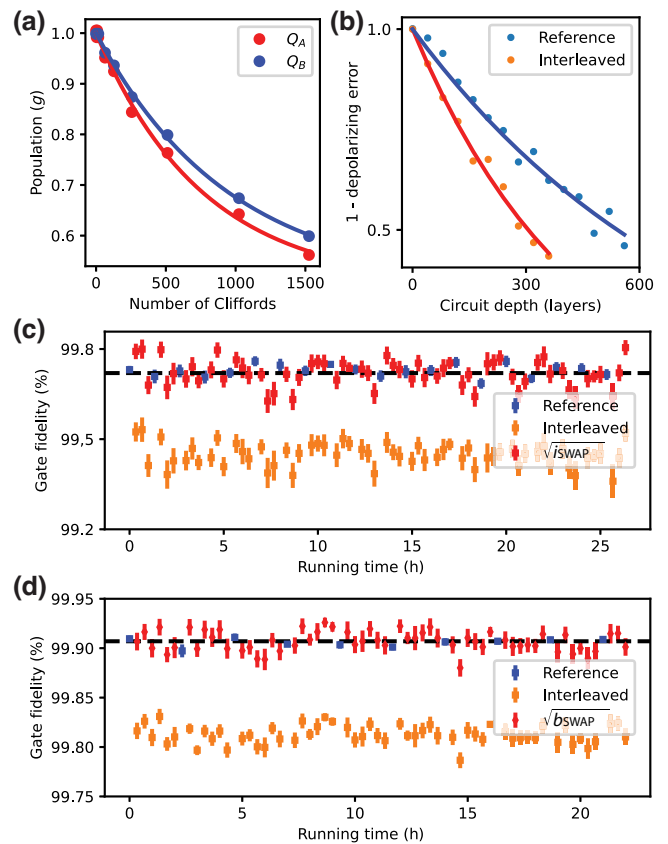


FIG. 4. The measured single- and two-qubit gate fidelities. (a) Simultaneous single-qubit randomized benchmarking. The average single-qubit Clifford-gate fidelity of qubit  $A$  (qubit  $B$ ) is 99.94% (99.95%). (b) Cross-entropy benchmarking data, where “Reference” consists of layers of single-qubit gates and “Interleaved” includes an interleaved  $\sqrt{bswap}$  gate. The depolarizing error is extracted following the procedure in Ref. [39]. The “Reference” gate fidelity is 99.90% and the “Interleaved” gate fidelity is 99.83%. This results in a  $\sqrt{bswap}$  gate fidelity of 99.93%. (c)  $>25$ -h-long consecutive cross-entropy benchmarking runs for  $\sqrt{i\text{swap}}$  gates, showing an average gate fidelity (dashed line) of 99.72%. The error bars per point indicate the statistical-fit uncertainty. (d)  $>20$ -h-long consecutive cross-entropy benchmarking runs for  $\sqrt{bswap}$  gates, showing an average gate fidelity (dashed line) of 99.91%.

choices for our native two-qubit gates are

$$\begin{aligned}\sqrt{i\text{swap}} &= \begin{pmatrix} 1 & 0 & 0 & 0 \\ 0 & 1/\sqrt{2} & i/\sqrt{2} & 0 \\ 0 & i/\sqrt{2} & 1/\sqrt{2} & 0 \\ 0 & 0 & 0 & 1 \end{pmatrix}, \\ \sqrt{bswap} &= \begin{pmatrix} 1/\sqrt{2} & 0 & 0 & i/\sqrt{2} \\ 0 & 1 & 0 & 0 \\ 0 & 0 & 1 & 0 \\ i/\sqrt{2} & 0 & 0 & 1/\sqrt{2} \end{pmatrix}. \quad (3)\end{aligned}$$

These gates are fully entangling and have been used in demonstrating quantum advantage [1]. Furthermore, by embedding a  $\pi$  pulse between  $\sqrt{i\text{SWAP}}$  or  $\sqrt{b\text{SWAP}}$  gates, we can compile controlled-NOT (CNOT) and controlled-Z (CZ) gates while also echoing out low-frequency noise.

Using data shown in Fig. 3, we calibrate a  $\sqrt{i\text{SWAP}}$  ( $\sqrt{b\text{SWAP}}$ ) gate that takes 257.8 ns (101.6 ns). Because the drive frequency of  $\sqrt{i\text{SWAP}}$  ( $\sqrt{b\text{SWAP}}$ ) is 13.4 MHz (110.2 MHz), there are only four (11) oscillation periods in a single gate pulse. In the case of the  $\sqrt{i\text{SWAP}}$  pulse, the use of a shorter gate length causes the carrier-envelope phase to affect the energy of the pulse (see Appendix J2).

These two-qubit gates have three phase degrees of freedom, which can be calibrated by applying two virtual single-qubit  $Z_\phi$  gates as well as adjusting the coupler drive phase. We amplify the error associated with miscalibrated phases using specially designed sequences, allowing us to execute a pure  $\sqrt{i\text{SWAP}}$  or  $\sqrt{b\text{SWAP}}$  gate. This calibration method is detailed in Appendix I.

We measure the two-qubit gates using process tomography but this method is limited in fidelity precision by our state-preparation and -measurement (SPAM) errors [40] to be 95% (see Appendix I). Therefore, we perform a more precise gate-fidelity measurement by amplifying gate errors and using other methods, such as cross-entropy benchmarking [1,41] and interleaved randomized benchmarking [42].

We implement cross-entropy benchmarking by interleaving  $\sqrt{i\text{SWAP}}$  ( $\sqrt{b\text{SWAP}}$ ) gates between random single-qubit gates. To subtract the errors of the single-qubit gates, we first measure a reference sequence that has the same number of layers, where each layer consists of a  $\pi/2$  gate and a  $Z$  gate on each qubit, both with randomly selected phases ( $\phi = n\pi/4, n \in [0, 7]$ ). The depolarizing error [39,41] is found by varying the number of layers and measuring the qubit state population. Then, we repeat the process with the interleaved sequence. Because the reference gates are randomly sampled, we can calculate the depolarizing error of the two-qubit gate as  $p = p_{\text{interleaved}}/p_{\text{reference}}$ . We subsequently find the gate fidelity from the gate depolarizing error with

$$F = p + (1 - p)/D, \quad (4)$$

where  $p$  is the depolarizing error of the two-qubit gate,  $D$  is the dimension of the Hilbert space, and  $F$  is the gate fidelity.

We continuously perform cross-entropy benchmarking for both  $\sqrt{i\text{SWAP}}$  and  $\sqrt{b\text{SWAP}}$  gates for more than 20 h, as shown in Fig. 4. For  $\sqrt{i\text{SWAP}}$ , we interleave it in reference sequences consisting of single-qubit gates made of Gaussian pulses. We measure an average reference sequence depolarizing error of approximately  $3.2 \times 10^{-3}$  and an average interleaved sequence depolarizing error of approximately  $6 \times 10^{-3}$ . Using Eq. 4, we derive an average

$\sqrt{i\text{SWAP}}$  fidelity  $99.72 \pm 0.04\%$ . For  $\sqrt{b\text{SWAP}}$ , we implement DRAG pulses on the single-qubit gates to improve the reference sequence fidelity. We measure a depolarizing error of approximately  $1.3 \times 10^{-3}$  of the reference sequences and a total depolarizing error of approximately  $2.4 \times 10^{-3}$  of the interleaved sequences, which results in a  $\sqrt{b\text{SWAP}}$  gate fidelity  $99.91 \pm 0.01\%$ .

We compute the error budget of our single- and two-qubit gates, taking into account decoherence and other error channels, in Table II. For all gates, qubit decoherence is the dominant source of error, while the beyond rotating-wave approximation (RWA) errors and carrier-envelope errors caused by using slow qubits are much lower, which shows the feasibility of high-fidelity gates within the low-frequency regime.

Finally, we construct a CNOT gate with two  $\sqrt{b\text{SWAP}}$  gates and five single-qubit gates and measure a CNOT fidelity of 99.5% with two-qubit interleaved randomized benchmarking. This result is consistent with our previously measured single-qubit and  $\sqrt{b\text{SWAP}}$  gate fidelities and can be further improved with better circuit compilation.

## V. CONCLUSIONS

We have presented a tunable coupler design for heavy-fluxonium qubits, which utilizes inductive coupling to take advantage of the large phase matrix elements. This coupler can achieve strengths that rival the single-qubit energies and can also be turned off, nulling the coupling strength to much less than the coherence time. The qubits retain high coherences and high fidelity of single-qubit gates ( $>99.94\%$ ) from simultaneous randomized benchmarking. We have demonstrated fast high-fidelity  $\sqrt{i\text{SWAP}}$  and  $\sqrt{b\text{SWAP}}$  gates by parametrically driving the coupler and we have achieved over 99.9% two-qubit gate fidelity for the  $\sqrt{b\text{SWAP}}$  gate.

In this architecture, all gate operations take place fully within the computational subspace, without occupation of higher levels. All gate operations use moderate-frequency rf pulses ranging from approximately 10 MHz to 100 MHz, which can easily be synthesized by direct digital synthesis. These demonstrated advantages can help explore a new regime of circuit design and gate schemes in the future.

## ACKNOWLEDGMENTS

We would like to thank Sho Uemera, Leandro Stefanazzi, and Gustavo Cancelo for their help with the RFSoC, and Kevin He, Kan-Heng Lee, Ziqian Li, Tanay Roy, and Rachel Dey for useful discussions. This work was supported by the Army Research Office under Grant No. W911NF1910016. This work is funded in part by Enabling Practical-Scale Quantum Computation (EPiQC), a National Science Foundation (NSF) Expedition in Computing, under Grant No. CCF1730449. This work was

partially supported by the University of Chicago Materials Research Science and Engineering Center, which is funded by the NSF under Award No. DMR-1420709. The devices were fabricated in the Pritzker Nanofabrication Facility at the University of Chicago, which receives support from the Soft and Hybrid Nanotechnology Experimental (SHyNE) Resource (NSF ECCS-1542205), a node of the NSF's National Nanotechnology Coordinated Infrastructure. S.S. was supported by the Department of Defense (DoD) through the National Defense Science & Engineering Graduate Fellowship (NDSEG) Program.

## APPENDIX A: FULL CIRCUIT MODEL

The full Hamiltonian of the circuit shown in Fig. 1(b) is  $H = H_{\text{qubit}} + H_{\text{coupler}} + V$ , where

$$H_{\text{qubit}} = \sum_{\mu=A,B} [4E_{C\mu}n_{\mu}^2 + \frac{1}{2}E_{L\mu}\varphi_{\mu}^2 + E_{J\mu} \cos(\varphi_{\mu} + \pi)], \quad (\text{A1a})$$

$$\begin{aligned} H_{\text{coupler}} = & 4E_{C-}n_{-}^2 + \frac{1}{2}E_{LC}\varphi_{-}^2 - E_{Jc} \cos(\varphi_{-} + 2\pi\Phi_c/\Phi_0) \\ & + 4E_{C+}n_{+}^2 + \frac{1}{2}E_{LC}\varphi_{+}^2, \end{aligned} \quad (\text{A1b})$$

$$\begin{aligned} V = & -\frac{E_{LA}}{2}[\varphi_a(\varphi_{+} + \varphi_{-})] - \frac{E_{LB}}{2}[\varphi_b(\varphi_{+} - \varphi_{-})] \\ & + \sum_{\mu=A,B} \frac{E_{L\mu}}{2}\delta\phi_{\mu}[-2\varphi_{\mu} + \varphi_{+} + (-1)^{\mu}\varphi_{-}], \end{aligned} \quad (\text{A1c})$$

in which  $[\varphi_{\mu}, n_{\nu}] = i\delta_{\mu\nu}$ ,  $\mu = A, B, -, +$ , and we have defined  $E_{LC} = \frac{1}{2}(\frac{1}{2}[E_{LA} + E_{LB}] + E_L)$ ,  $E_{C+} = 2E_{Cc}$ , and  $E_{C-} = (1/E_{Cm} + 1/[2E_{Cc}])^{-1}$ . All other circuit parameters can be read off from Fig. 1(b). To account for the need to tune the qubit flux as a function of the coupler flux, as discussed in the main text, we define  $\delta\phi_{\mu} = \phi_{\mu} - \pi$ . For further details on the derivation of Eq. (A1), see Ref. [27].

We comment briefly on how the effective Hamiltonian Eq. (2) arises from Eq. (A1). The  $XX$  operator content of the effective coupling between the qubits can be traced back to the operator form of the coupling between the qubits and the couplers,  $\varphi_{\mu}\varphi_{\pm}$ . The phase operator in the qubit subspace of a fluxonium qubit biased at the sweet spot can be written as  $\langle 1|\varphi|0\rangle\sigma_x$  [12]. Thus, one application of the perturbing term  $\varphi_a\varphi_{\pm}$  swaps, e.g., an excitation of qubit  $A$  into the coupler and an application of  $\varphi_b\varphi_{\pm}$  returns this excitation to the qubit subspace in the form of an excitation of qubit  $B$  (for further details, see Ref. [27]).

Using this Hamiltonian, we locate the sweet-spot contour by minimizing the eigenenergy  $E_{1100}$  as a function of the qubit fluxes, keeping the coupler flux fixed. The

off position is then found by performing the same minimization along the sweet-spot contour as a function of the coupler flux.

## APPENDIX B: PLASMON SPECTROSCOPY AND FULL MODEL FITTING

To determine the physical parameters of our system, we measure the two-tone spectroscopies of higher-frequency (approximately 5 GHz) transitions. Each qubit is charge driven through the readout resonator while the resonator is being probed. We see a sharp change in the resonator transmission when a qubit transition is driven on resonance. Thus, by sweeping different flux biases, we can see a frequency-flux 2D qubit spectroscopy. We measure the transition frequencies from the ground state to first and second plasmon states ( $|20\rangle$  and  $|30\rangle$ ) for qubit  $A$  while changing the qubit- $A$  flux bias. Because  $|10\rangle$  has significant thermal population around the  $\Phi_{\text{ext},A} = 0.5\Phi_0$  bias point, we can also see transitions from it to the higher levels [see Fig. 5(a)]. Similarly, we measure transition frequencies for qubit  $B$  [see Figs. 5(b) and 5(c)]. Using the SCQUBITS software package [43,44], we subsequently fit the spectroscopy data with the full Hamiltonian Eq. (A1), as shown in overlay lines in Fig. 5. Because our dc-flux crosstalk matrix is not perfectly calibrated across this range, we cannot keep the coupler and the other qubit flux biases precisely at the same point during a flux sweep, leading to slight mismatches between the theory curves and experimental data.

## APPENDIX C: ZZ SUPPRESSION

The suppression of static  $ZZ$  coupling is an attractive feature of our architecture, allowing for large on-off ratios. This suppression is achieved by cancelling out two contributions of  $ZZ$  by fine tuning the qubit flux bias. To see this, we start from the effective Hamiltonian

$$H_{\text{eff}} = -\sum_{\mu=A,B} \frac{\omega_{\mu}}{2}\sigma_z^{\mu} - \Omega_{\mu}\sigma_x^{\mu} + J\sigma_x^A\sigma_x^B + \zeta\sigma_z^A\sigma_z^B, \quad (\text{C1})$$

where the Pauli operators are defined in the eigenbasis of the system at the off position. The static  $ZZ$  shift  $\zeta$  is small for a number of reasons. First,  $\zeta$  is generally suppressed in low-frequency fluxonium architectures, due to the large detuning between the qubit excitation energies and the energies of the higher-lying states [18]. Second, the galvanic coupling architecture helps suppress  $\zeta$  because the phase matrix elements of qubit states with higher-lying fluxonium states are very small relative to charge matrix elements. Finally, there is no direct coupling between the qubits in this architecture. Thus, second- and third-order contributions to  $\zeta$  vanish, with the leading-order contribution arising only at fourth order in perturbation theory

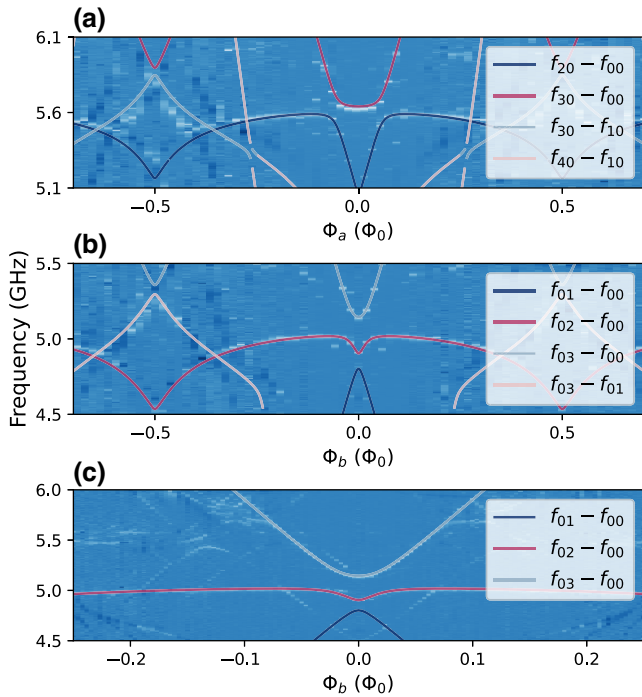


FIG. 5. The plasmon-spectroscopy features of both qubits. (a) The  $|00\rangle \rightarrow |20\rangle$  and  $|00\rangle \rightarrow |30\rangle$  transition frequency versus the qubit-*A* flux bias. (b) The  $|00\rangle \rightarrow |02\rangle$  and  $|00\rangle \rightarrow |03\rangle$  transition frequency versus the qubit-*B* flux bias. (c) An enlargement of the plot around  $\Phi_{ext,B} = 0$ . The data were taken with the coupler flux around 0 and the flux of the other qubit fixed at 0.

[9,17,45]. Sweeping the coupler flux while keeping qubits at their sweet spots ( $\Omega_\mu = 0$ ),  $|\zeta|$  is nonvanishing and on the order of 1 kHz.

However,  $\zeta$  can be canceled with a nonzero  $\Omega_\mu$  by qubit-flux-dependent shifts away from the sweet-spot contour. To see this, we diagonalize the single-qubit terms in Eq. (C1) up to second order of  $\Omega_\mu/\omega_\mu$  using the unitary transformation  $U = \exp(-i \sum_{\mu=A,B} (\Omega_\mu/\omega_\mu) \sigma_y^\mu)$ , yielding

$$H'_{\text{eff}} = U^\dagger H_{\text{eff}} U = - \sum_{\mu=A,B} \frac{\omega_\mu + 2\frac{\Omega_\mu^2}{\omega_\mu}}{2} \sigma_z^\mu + J \left( \sigma_x^A + \frac{2\Omega_A}{\omega_A} \sigma_z^A \right) \left( \sigma_x^B + \frac{2\Omega_B}{\omega_B} \sigma_z^B \right) + \zeta \sigma_z^A \sigma_z^B, \quad (\text{C2})$$

where we have expanded the result to second order in the small parameters  $\Omega_\mu/\omega_\mu$  and ignored negligible corrections arising from the last term in Eq. (C2). Thus the

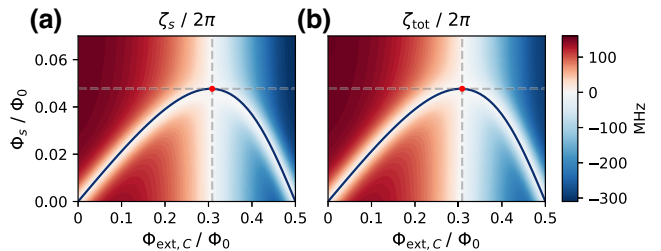


FIG. 6. The ZZ interaction strength (a)  $\zeta_s$  obtained from the effective model and (b)  $\zeta_{tot}$  from numerical diagonalization of the full model. Both quantities are plotted as a function of the qubit flux shifts  $\Phi_s \equiv \Phi_{ext,A} - 0.5\Phi_0 = 0.5\Phi_0 - \Phi_{ext,B}$  and the coupler flux  $\Phi_{ext,C}$ . In both plots, the red circle marks the off position and the solid curves are the “sweet-spot contours.” We find that  $\zeta_s$  is the main contributor to  $\zeta_{tot}$  and that  $\zeta_s$  can be tuned from positive to negative values to cancel out  $\zeta$ .

overall ZZ shift is given by  $\zeta_{tot} = \zeta + \zeta_s$ ,

$$\zeta_s = J \frac{4\Omega_A \Omega_B}{\omega_A \omega_B}, \quad (\text{C3})$$

where both contributions effectively arise as fourth-order perturbations. The sign of  $\zeta_s$  depends upon the signs of  $J$  and  $\Omega_\mu$ , where, notably,  $J$  changes sign when moving across the off position in coupler flux [see Fig. 6(a)]. Thus with small adjustments in the qubit fluxes (so that the  $\Omega_\mu$  are nonzero) and the coupler flux,  $\zeta_s$  can be used to cancel  $\zeta$ . This leads to an overall vanishing ZZ shift  $\zeta_{tot} = 0$ .

We validate this understanding by calculating  $\zeta_{tot}$  using the full Hamiltonian (A1)

$$\zeta_{tot}/2\pi = f_{11} - f_{01} - f_{10} + f_{00}, \quad (\text{C4})$$

[see Fig. 6(b)]. The off position and  $\zeta_{tot} = 0$  point are within  $10^{-5}\Phi_0$  in the qubit fluxes according to the full model, relaxing the constraint of operating exactly on the sweet-spot contour. We need not worry about tuning of the qubit fluxes away from the sweet spot, as flux tuning at the  $10^{-5}\Phi_0$  level is below the resolution of our dc bias source and contributes minimally to flux-noise induced dephasing.

#### APPENDIX D: EFFECTS DUE TO rf-FLUX CROSSTALK

In the presence of rf-flux crosstalk, where flux penetrates each of the qubit loops when we drive the coupler, dynamic effects arise that reduce the gate fidelity. For simplicity, we ignore the effects of the Gaussian envelope of the pulse in this appendix. The Hamiltonian of the system is

$$H_{\text{eff,ct}} = - \sum_{\mu=A,B} \left( \frac{\omega_\mu}{2} \sigma_z^\mu + \Omega_{ct,\mu} \cos(\omega_{dt} t) \sigma_x^\mu \right) + J_{\text{ac}} \cos(\omega_{dt} t) \sigma_x^A \sigma_x^B, \quad (\text{D1})$$

where  $\Omega_{\text{ct},\mu}$  describes the maximum qubit-flux drive amplitude due to crosstalk. The drive frequency will typically be set to  $f_d \approx f_{01} - f_{10}$  for an  $\sqrt{i}$ SWAP-style gate or  $f_d \approx f_{01} + f_{10}$  for a  $\sqrt{b}$ SWAP-style gate, with  $\omega_d = 2\pi f_d$ . In each case, the drives are detuned from single-qubit transition frequencies. This unwanted drive thus dynamically shifts the qubit frequencies rather than inducing Rabi oscillations [46]. To see this, we first move to a frame rotating at the drive frequency. Making the RWA for the single-qubit drive terms while keeping all terms associated with the two-qubit drive, we obtain

$$\begin{aligned} H'_{\text{eff,ct}} = & - \sum_{\mu=A,B} \left( \frac{\omega_\mu - \omega_d}{2} \sigma_z^\mu + \frac{\Omega_{\text{ct},\mu}}{2} \sigma_x^\mu \right) \\ & + J_{\text{ac}} \cos(\omega_d t) (\cos(\omega_d t) \sigma_x^A + \sin(\omega_d t) \sigma_y^A) \\ & \times (\cos(\omega_d t) \sigma_x^B + \sin(\omega_d t) \sigma_y^B). \end{aligned} \quad (\text{D2})$$

As in Sec. C, we diagonalize the single-qubit terms in Eq. (D2) to second order in  $\Omega_{\text{ct},\mu}/(\omega_\mu - \omega_d)$ , yielding

$$\begin{aligned} H''_{\text{eff,ct}} = & - \sum_{\mu=A,B} \frac{\omega_\mu + \delta\omega_\mu}{2} \sigma_z^\mu + J_{\text{ac}} \cos(\omega_d t) \\ & \left( \sigma_x^A + \frac{\Omega_{\text{ct},A}}{\omega_A - \omega_d} \sigma_z^A \right) \left( \sigma_x^B + \frac{\Omega_{\text{ct},B}}{\omega_B - \omega_d} \sigma_z^B \right), \end{aligned} \quad (\text{D3})$$

where  $\delta\omega_\mu = \Omega_{\text{ct},\mu}^2/2(\omega_\mu - \omega_d)$  and we have returned to the laboratory frame. Thus, the leading-order effects of ac-flux crosstalk are to renormalize the qubit frequencies as well as modify the effective two-qubit drive term from  $XX$  to a combination of  $XX$ ,  $ZX$ ,  $XZ$ , and  $ZZ$ . To avoid these unwanted dynamic effects, it is thus critical to cancel geometric flux crosstalk. We discuss the quantitative contribution of ac-flux crosstalk to gate infidelities in Appendix J.

## APPENDIX E: EXPERIMENTAL SETUP

The experiment is performed in a Bluefors LD-250 dilution refrigerator with the wiring configured as shown in Fig. 7. The flux and charge inputs are attenuated at the 4-K stage and the mixing chamber with standard XMA attenuators, except the final 20-dB attenuator on the rf charge line (threaded copper). The dc- and rf-flux signals are combined in a bias tee (Mini-Circuits® ZFBT-4R2GW+), where the coupler bias tee is modified such that the capacitor is replaced with a short to further lower the high-pass cutoff frequency. The dc- and rf-flux lines included commercial low-pass filters (Mini-Circuits®) as indicated. The rf-flux and output lines also have additional low-pass filters with a sharp cutoff (8 GHz) from K&L microwave. Home-made Eccosorb (CR110) IR filters are added on the flux, input, and output lines, which further improves

the  $T_1$  and  $T_2$  coherences and reduces the qubit and resonator temperatures. The device is heat sunk to the base stage of the dilution refrigerator (stabilized at 15 mK) via an oxygen-free high-conductivity (OFHC) copper post, while surrounded by an inner lead shield thermalized via a welded copper ring. This is additionally surrounded by two cylindrical  $\mu$ -metal cans (MuShield), thermally anchored using an inner close-fitting copper-shim sheet, attached to the copper can lid. We ensure that the sample shield is light tight, to reduce thermal photons from the environment.

## APPENDIX F: DEVICE FABRICATION

The device (shown in Fig. 1 in the main text) is fabricated on a 430- $\mu$ m-thick C-plane sapphire substrate. The base layer of the device, which includes the majority of the circuit (excluding the Josephson junctions), consists of 200 nm of tantalum with features fabricated via optical lithography and HF etch at wafer scale.

We perform standard cleaning using toluene, acetone, methanol, and isopropyl alcohol (TAMI) on the annealed sapphire substrates, followed with nanostrip etching at 50 °C for 10 min, and sulfuric acid etching at 140 °C for 10 min. We subsequently deposit 200 nm tantalum in an AJA ATC 2200 sputtering tool at 800 °C. A 2000-nm-thick layer of AZ 1518 is used as the (positive) photoresist and the large features are written using a Heidelberg MLA 150 Direct Writer. After 60 s of development with MIF 300 and a 10 min oven bake at 120 °C, we perform 20 s of HF etching using Ta etchant 1:1:1 (Transene Tantalum Etchant 111).

The junction mask is fabricated via electron-beam lithography with a bilayer resist (MMA-PMMA) comprised of MMA EL11 and 495 PMMA A6 spun at 4000 RPM. The e-beam lithography is performed on a 100 kV Raith EBPG5000 Plus E-Beam Writer. All Josephson junctions are made with the Dolan-bridge technique and etched for 2 min using a 3:1 DI:IPA solution at 6 °C. Aluminum was subsequently evaporated onto the chip in a Plassys electron-beam evaporator using double-angle evaporation ( $\pm 21^\circ$ ), first depositing a 70-nm Al layer, performing static oxidation, and subsequently depositing a 90-nm Al layer. The wafer is then diced into  $7 \times 7$  mm chips, mounted on a printed circuit board, and subsequently wire bonded.

## APPENDIX G: READOUT AND ACTIVE RESET

We utilize the active-feedback capabilities of the Xilinx RFSoc field-programmable gate array (FPGA) board with the QICK open-source control code base. We perform simultaneous dispersive readout, using readout lengths of 10.4 and 18.2  $\mu$ s, respectively. The readout data are then processed on the FPGA board and compared to a previously calibrated threshold and the board conditionally plays a single-qubit  $\pi$  pulse to initialize the qubit to its ground state.

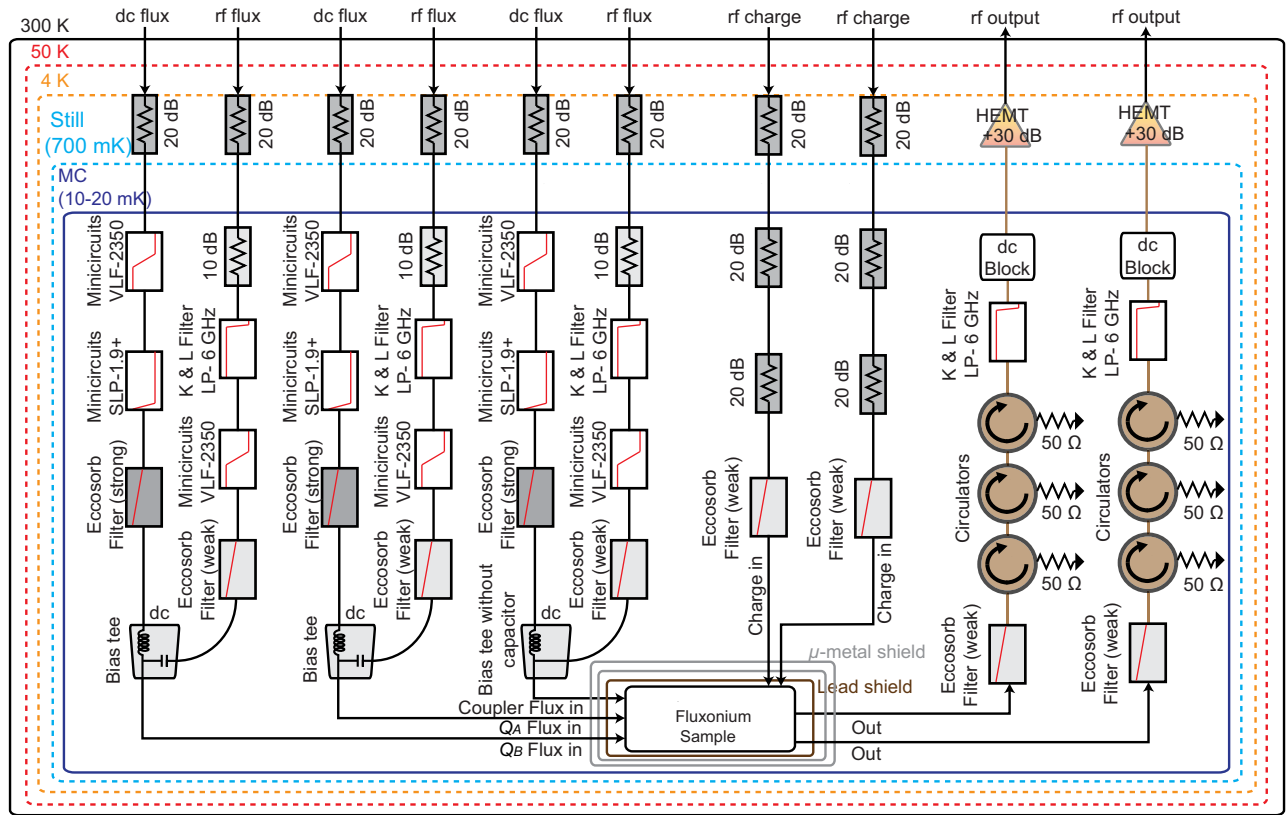


FIG. 7. The wiring diagram inside the dilution refrigerator. Outside the dilution fridge, there is 13–20 dB of attenuation and a dc block on the rf-flux line and an ultra-low-pass (<1 Hz)  $RC$  filter on the dc-flux line. Adding attenuation on the rf-flux lines at room temperature leads to a measured increase in the  $T_1$  and  $T_2$  coherences of the qubits. MC refers to mixing chamber.

We first take 10 000 readouts with the qubit uninitialized at the sweet spot. Because the Boltzmann temperature of the qubit (<2.8 mK) is lower than the temperature of the environment, we expect to see the qubit in thermal equilibrium. Indeed, we see approximately a 50:50 population split between the ground and excited states. Using a double-Gaussian function, we fit the data to determine the demarcation line that best classifies the qubit state for use in readout and active reset.

We measure our reset fidelity by initializing the qubit in  $|g\rangle$  and  $|e\rangle$  using active reset and then take another measurement right after the reset to obtain histogram shown in Fig. 8. We extract postselected active reset fidelities of 93% and 95%, respectively, for each qubit, this being very close to the readout fidelities due to the fast feedback time and high-fidelity single-qubit  $\pi$  pulse. By fitting the thermal population of the qubit ground and excited states, we can also measure the qubit temperatures to be approximately 50 mK.

## APPENDIX H: FLUX-CROSSTALK CALIBRATIONS

The dc- and rf-flux crosstalk of the system are significant and require calibration to mitigate unwanted effects

that degrade gate fidelity. We measure the dc-flux crosstalk by performing 2D flux sweeps for different pairs of flux lines while probing the resonator. This reveals sharp

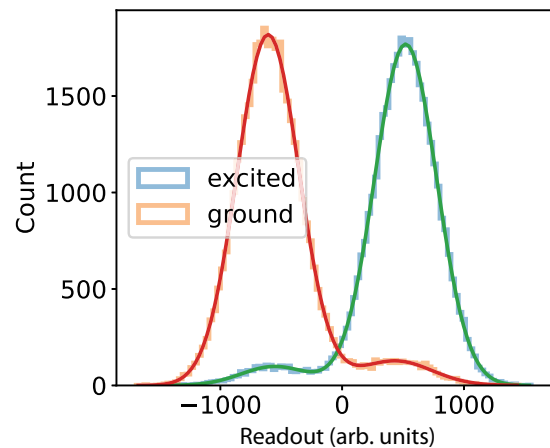


FIG. 8. A histogram of the readout data after initializing the qubit in either the ground or the excited state via active reset. The populations are then fitted to a double-Gaussian function and subsequently plotted as red and green solid lines. This fit is analyzed to determine the qubit temperature.

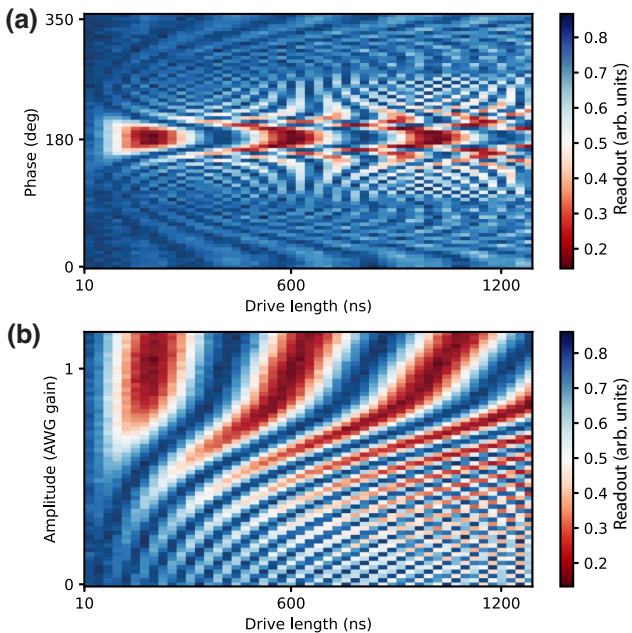


FIG. 9. (a) Performing a drive at the sum of qubit frequencies with various lengths while sweeping the phase of a cancellation pulse. The amplitude of this sweep is randomly chosen but it needs to be lower than the correct cancellation amplitude. (b) With the phase calibrated in (a), performing a drive at the sum of qubit frequencies with various lengths while sweeping the amplitude of a cancellation pulse.

flux-dependent features that originate from bringing qubit energy levels on resonance with the readout resonator. The slope of these lines is the dc-flux crosstalk of our system.

To minimize rf-flux crosstalk, we use compensation pulses that are played at the same time as the original drive pulse. These compensation pulses have the same length as the original pulse but we tune the phase and amplitude of these pulses to minimize the effect of flux crosstalk. Since the phases of these compensation pulses are independent parameters, we first calibrate them individually. Because the flux crosstalk can be understood as an off-resonant qubit drive, we would observe an ac Stark-shifted qubit frequency when performing a Rabi experiment. We Rabi drive at the  $\sqrt{b_{SWAP}}$  frequency, which is the sum of bare-qubit frequencies. The Rabi contrast is maximized when the qubit frequency shift is minimized, making this a good metric for measuring rf crosstalk. Therefore, we sweep the phase of the compensation pulse while playing it simultaneously with the drive pulse, as shown in Fig. 9(a). The maximum Rabi contrast of the  $|00\rangle \leftrightarrow |11\rangle$  oscillation determines the correct compensation pulse phase.

After fixing the correct phases for both compensation channels, we determine the optimal cancellation pulse amplitudes in a similar sweep. As before, we look for the maximum Rabi contrast of the  $|00\rangle \leftrightarrow |11\rangle$  oscillation but, in this case, we sweep the amplitude of the compensation

pulse, shown in Fig. 9(b). Because the cancellation gains from the two qubit channels will affect each other, we do this iteratively to find the optimal amplitudes for both of them.

Due to the linear nature of the flux crosstalk, the amplitudes of the drive and compensation pulses have a linear relationship and the phase difference between all three pulses is not amplitude dependent. With cancellation phases and amplitudes for one drive pulse calibrated, we can utilize this procedure to find compensation pulses for all  $|00\rangle \leftrightarrow |11\rangle$  drive pulses. The two-qubit gates reported in this paper are all constructed in this way, with the coupler drive pulse and cancellation pulses on each qubit.

## APPENDIX I: TWO-QUBIT-GATE CALIBRATIONS

We calibrate the  $\sqrt{i_{SWAP}}$  and  $\sqrt{b_{SWAP}}$  gates with gate sequences designed to amplify the gate errors. The gate calibration process consists of two steps, the rotation-angle calibration and phase calibrations. We can write the Hermitian matrix for a gate generated by a generic  $XX$  parametric drive on the coupler as

$$\sqrt{\phi_b SWAP} = \begin{pmatrix} \cos \theta & 0 & 0 & ie^{i\phi_D} \sin \theta \\ 0 & e^{i\phi_{01}} & 0 & 0 \\ 0 & 0 & e^{i\phi_{10}} & 0 \\ ie^{i(\phi_{11}-\phi_D)} \sin \theta & 0 & 0 & e^{i\phi_{11}} \cos \theta \end{pmatrix} \quad (11)$$

for  $|00\rangle \leftrightarrow |11\rangle$  oscillation and

$$\sqrt{\phi_i SWAP} = \begin{pmatrix} 1 & 0 & 0 & 0 \\ 0 & e^{i\phi_{01}} \cos \theta & ie^{i(\phi_{01}+\phi_D)} \sin \theta & 0 \\ 0 & ie^{i(\phi_{10}-\phi_D)} \sin \theta & e^{i\phi_{10}} \cos \theta & 0 \\ 0 & 0 & 0 & e^{i\phi_{11}} \end{pmatrix} \quad (12)$$

for  $|01\rangle \leftrightarrow |10\rangle$  oscillation, where  $\phi_D$  is the phase of the coupler drive,  $\phi_{01}$ ,  $\phi_{10}$ , and  $\phi_{11}$  are phases due to the frequency shift of levels while the drive is on, which have the relationship  $\phi_{11} = \phi_{01} + \phi_{10} + \phi_{zz}$  [47]. In our system, since all frequency shifts and the ZZ term during the parametric drive are small, we have  $\phi_{11} \approx \phi_{01} + \phi_{10}$  and all of  $\phi_{01}$ ,  $\phi_{10}$ , and  $\phi_{11}$  are close to 0. We first calibrate the rotation angle ( $\theta$ ). We fix the pulse length for  $\sqrt{i_{SWAP}}$  at  $99\,000/384 \approx 257.8$  ns and for  $\sqrt{b_{SWAP}}$  at  $39\,000/384 \approx 101.6$  ns. Since our arbitrary wave-form generator (AWG) (Xilinx RFSoC) has a 384-MHz processor, the pulse lengths are integer multiples of  $1000/384$  ns. We initialize the system in state  $|00\rangle$ , sweep the pulse amplitude while playing the same pulse consecutively  $4n + 2$  times, and look for the amplitude that gives us the highest-fidelity  $|11\rangle$  state. By playing the same gate for up to 402 times, we can obtain the value of parameter  $\theta$  up to  $1 \times 10^{-4}$  in precision.

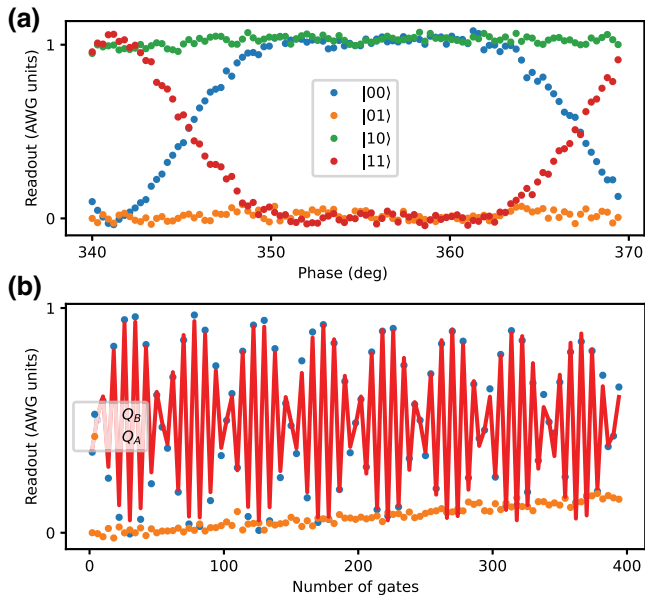


FIG. 10. (a) Playing the pulse sequence in Fig. 12 while sweeping the phase of qubit-*A* phase gates ( $Z_A$ ). At  $\phi_A = 357^\circ$ , the phase of  $\phi_{01} + \phi_{10}$  is perfectly cancelled; thus  $\phi_{01} + \phi_{10} = 3$ . (b) Playing the pulse sequence in Fig. 13 with various copies of the  $\sqrt{bSWAP}$  gates and measuring the final state of both qubits. With this sequence, qubit *A* should only see a decay process to thermal equilibrium and the qubit-*B* state dependence on the number of gates is shown in Eqs. 13. By fitting the data, we can extract the value of  $\phi_{01}$  and  $\phi_{10}$ .

With  $\theta$  calibrated to be  $\pi/4$ , gate phases  $\phi_{01}$ ,  $\phi_{10}$ ,  $\phi_{11}$ , and  $\phi_D$  are subsequently calibrated. Since the calibration process is very similar for  $\sqrt{iSWAP}$  and  $\sqrt{bSWAP}$  gates, here we only use  $\sqrt{bSWAP}$  as an example for explanation. We calibrate these phases with the sequence shown in Fig. 12, where  $Z_A$  and  $Z_B$  are single-qubit phase gates on each qubit with phase  $\phi_A$  and  $\phi_B$ . A unit consists of one  $\sqrt{bSWAP}$  gate and two single-qubit  $Z$  gates, and we note that with  $4n + 2$  units, it is only when  $\phi_A + \phi_B = -\phi_{11}$  that we obtain a  $bSWAP$  gate up to some phases. Thus we play a sequence of 321 units while sweeping  $\phi_A$  (shown in Fig. 10) and measure  $\phi_{11}$  to be around  $-3$  degrees. We subsequently play the sequence as shown in Fig. 13 and with  $4n + 2$  units, we have the qubit-*B* ground-state population,

$$\frac{1}{2}(1 + (-1)^n \sin(4n(\phi_{10} - \phi_{11}) + 2(\phi_{10} - \phi_{11}) + \phi_D)). \quad (I3)$$

The qubit-*A* ground-state population should always be 0 for all the  $n$  values. Fitting this function gives us  $\phi_{10} - \phi_{11}$  and  $2\phi_{10} - 2\phi_{11} + \phi_D$  (shown in Fig. 10). With the  $\phi_{11}$  value measured from the above step, we can derive  $\phi_{10}$ ,  $\phi_{11}$ , and  $\phi_D$ . Since  $\phi_{ZZ}$  is very small in our system, we can calculate  $\phi_{01}$  as  $\phi_{11} - \phi_{10}$  and the result is very close to

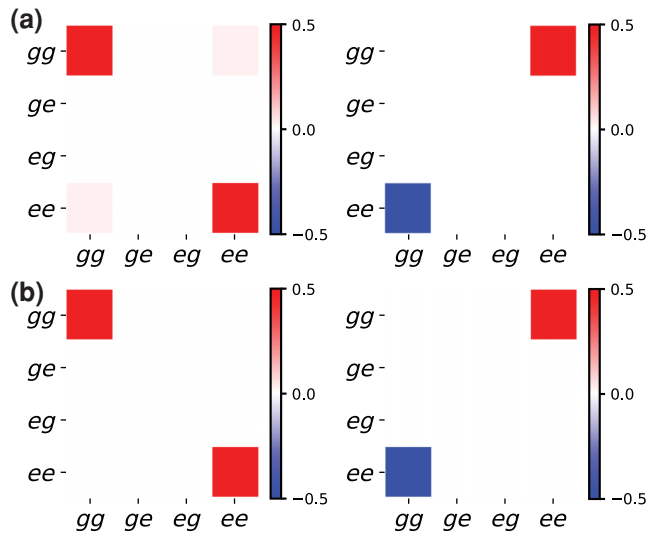


FIG. 11. Direct preparation of the  $|gg\rangle + i|ee\rangle$  Bell state using a  $\sqrt{iSWAP}$  gate on the initialized  $|gg\rangle$  state. (a) State tomography provides experimental data of the density matrix of this state. On the left is the real part and on the right is on the imaginary part. The purity and state fidelity are 95%, limited by SPAM errors. (b) The density matrix of the ideal  $|gg\rangle + i|ee\rangle$ , calculated using the theory, for comparison.

directly measuring  $\phi_{01}$  by switching operations on qubits *A* and *B*.

Using the calibrated values, we adjust the phases of the virtual  $Z$  gates following the parametric coupler drive, such that the qubit-*A*  $Z$  gate has phase  $\phi_A = -\phi_{10}$ , the qubit-*B*  $Z$  gate has phase  $\phi_B = -\phi_{01}$ , and the coupler drive has phase  $-\phi_D$ . In this experiment, all the single-qubit  $Z$  gates are virtual; therefore we only need to update the phase of the pulses after a  $\sqrt{bSWAP}$  or  $\sqrt{iSWAP}$  gate for each qubit. One characterization of our calibrated gate is done by executing quantum state tomography (QST). We prepare the Bell state  $|gg\rangle + i|ee\rangle$  using the application of a  $\sqrt{iSWAP}$  gate, as shown in Fig. 11. This measurement shows a state purity and state fidelity of 95%, limited by state preparation and measurement (SPAM) errors. Then, we execute quantum process tomography, performing QST measurements on the complete two-qubit basis states to extract the full process matrix, as shown in Fig. 14.

## APPENDIX J: ERROR BUDGETING

Various sources contribute to the single- and two-qubit gate infidelities, including qubit decay, heating, dephasing, carrier-envelope variations, beyond-RWA effects, and rf-flux crosstalk. In this appendix, we quantify the contribution of each error source to the infidelity via QuTiP simulations and analytical estimates (where possible).

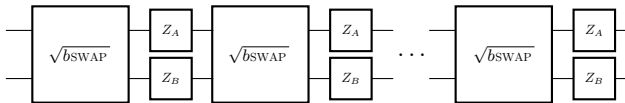


FIG. 12. The gate sequence for calibrating the  $\sqrt{b\text{SWAP}}$  gate phase  $\phi_{11}$ .

Simulations suggest that leakage to noncomputational states is negligible and attributable to the significant detuning between relevant drive frequencies and undesired transition frequencies. We can thus safely truncate the Hilbert space to the computational subspace. In the following, we focus on the specific example of error budgeting two-qubit gates, with similar results holding for single-qubit gates. In the presence of a coupler-flux drive, the laboratory-frame Hamiltonian is

$$H = -\frac{\omega_A}{2}\sigma_z^A - \frac{\omega_B}{2}\sigma_z^B + Af(t)\cos(\omega_dt + \theta_{\text{CE}})\sigma_x^A\sigma_x^B, \quad (\text{J1})$$

where  $A$  is the amplitude of the drive,  $f(t)$  is the Gaussian envelope, and  $\theta_{\text{CE}}$  is the carrier-envelope phase.

### 1. Beyond the RWA

Both qubits in our sample have Larmor periods of about 20 ns, only a slightly smaller time scale than the single- and two-qubit gates that we implement. Thus, it is possible that fidelities could begin to be limited by effects arising from counter-rotating terms. To obtain a semianalytical estimate of the associated fidelity reduction, we utilize a Magnus expansion [49–51] following Ref. [27]. Noting that the Hamiltonian only couples pairs of states  $|00\rangle \leftrightarrow |11\rangle$  and  $|01\rangle \leftrightarrow |10\rangle$ , we write the Hamiltonian (J3) as a direct sum  $H_{2q}(t) = H_-(t) \oplus H_+(t)$ , where

$$H_{\pm}(t) = -\frac{\omega_{\pm}}{2}\Sigma_z^{\pm} + Af(t)\cos(\omega_dt)\Sigma_x^{\pm}. \quad (\text{J2})$$

We define  $\omega_{\pm} = \omega_a \pm \omega_b$  and the Pauli matrices as, e.g.,  $\Sigma_x^+ = |00\rangle\langle 11| + \text{H.c.}$  and  $\Sigma_x^- = |01\rangle\langle 10| + \text{H.c.}$  For simplicity, we set  $\theta_{\text{CE}} = 0$  and postpone a discussion of carrier-envelope variations to Sec. J2. To isolate the effects of the drive, we move into a rotating frame, yielding

$$H'_{\pm}(t) = Af(t)\cos(\omega_dt)[\cos(\omega_{\pm}t)\Sigma_x^{\pm} + \sin(\omega_{\pm}t)\Sigma_y^{\pm}]. \quad (\text{J3})$$

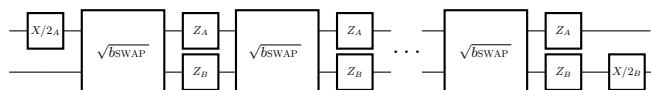


FIG. 13. The gate sequence for calibrating the  $\sqrt{b\text{SWAP}}$  gate phases  $\phi_{10}$  and  $\phi_D$ .

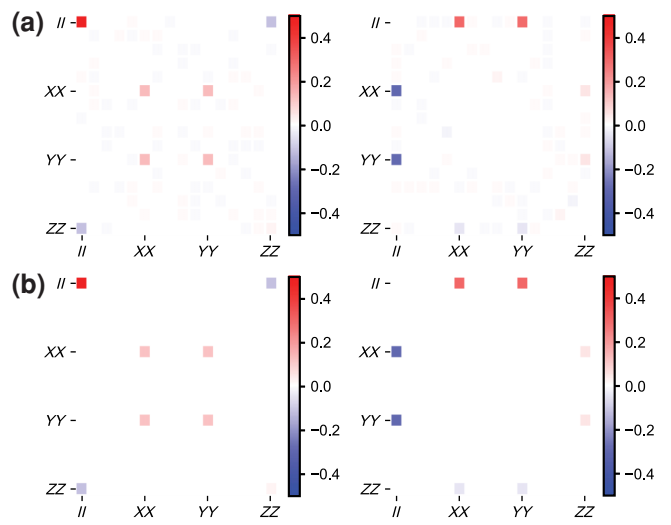


FIG. 14. (a) The experimental data of the process tomography on the  $\sqrt{i\text{SWAP}}$  gate, where the left side shows the real part and the right side shows the imaginary part. (b) The process tomography of an ideal  $\sqrt{i\text{SWAP}}$  gate, calculated using the theory.

Utilizing the first two terms in the Magnus expansion, the propagator is  $U_{2q}(t) = \exp(\Delta_1^-[t] + \Delta_1^+[t] + \Delta_2^-[t] + \Delta_2^+[t])$ , where [49–51]

$$\Delta_{1,\pm}(t) = -i \int_0^t H'_{\pm}(t') dt', \quad (\text{J4})$$

$$\Delta_{2,\pm}(t) = -\frac{1}{2} \int_0^t dt_1 \int_0^{t_1} dt_2 [H'_{\pm}(t_1), H'_{\pm}(t_2)]. \quad (\text{J5})$$

The gate time  $\tau$  is taken to be  $\tau = \sqrt{2\pi}/(A \text{erf}(\sqrt{2}))$ , appropriate to obtain a  $\sqrt{i\text{SWAP}}$  or  $\sqrt{b\text{SWAP}}$  in the RWA with Gaussian envelope  $f(t) = \exp(-0.5t^2/(\sigma^2))$  and width  $\sigma = \tau/4$ .

For the first terms in the Magnus expansion, we obtain

$$\begin{aligned} \Delta_{1,-}(\tau) + \Delta_{1,+}(\tau) &= -i\alpha_- \Sigma_x^- - i\alpha_+ \Sigma_x^+ \\ &= -i\frac{\alpha_-}{2}(\sigma_x^a \sigma_x^b + \sigma_y^a \sigma_y^b) \\ &\quad - i\frac{\alpha_+}{2}(\sigma_x^a \sigma_x^b - \sigma_y^a \sigma_y^b), \end{aligned} \quad (\text{J6})$$

where

$$\alpha_{\pm} = \int_0^{\tau} dt Af(t) \cos(\omega_dt) \cos(\omega_{\pm}t). \quad (\text{J7})$$

These terms describe the desired drive ( $\alpha_- = \pi/4, \alpha_+ = 0$  for  $\sqrt{i\text{SWAP}}$  and  $\alpha_+ = \pi/4, \alpha_- = 0$  for  $\sqrt{b\text{SWAP}}$ ) as well as an undesired term that causes transitions between, e.g.,

$|00\rangle \leftrightarrow |11\rangle$  in the case of  $\sqrt{i\text{SWAP}}$ . For the second-order terms, we obtain

$$\begin{aligned}\Delta_{2,-}(\tau) + \Delta_{2,+}(\tau) &= -i\beta_- \Sigma_z^- - i\beta_+ \Sigma_z^+ \\ &= -i\frac{\beta_+ + \beta_-}{2} \sigma_z^a - i\frac{\beta_+ - \beta_-}{2} \sigma_z^b,\end{aligned}\quad (\text{J8})$$

where

$$\begin{aligned}\beta_\pm &= A^2 \int_0^\tau dt_1 \int_0^{t_1} dt_2 f(t_1)f(t_2) \cos(\omega_d t_1) \cos(\omega_d t_2) \\ &\times [\cos(\omega_\pm t_1) \sin(\omega_\pm t_2) - \sin(\omega_\pm t_1) \cos(\omega_\pm t_2)].\end{aligned}\quad (\text{J9})$$

These terms describe the familiar Bloch-Siegert shift, where the resonance frequencies of both qubits are shifted by the coupler drive.

As an aside, we comment that we have just derived the propagator to second order for single-qubit gates with a drive on  $\sigma_x$  (returning to the usual Pauli-matrix notation for clarity),  $U_{1q}(t) = \exp(-i\frac{1}{2}\alpha\sigma_x - i\frac{1}{2}\beta\sigma_z)$ , dropping the subscripts on  $\alpha$  and  $\beta$ , and redefining  $\alpha$  and  $\beta$  with an additional factor of 2 for later convenience.

Returning to two-qubit gates, we now specialize to the case of  $\sqrt{i\text{SWAP}}$  with  $\omega_d = \omega_a - \omega_b$ . A similar analysis follows for  $\sqrt{b\text{SWAP}}$  with  $\omega_d = \omega_a + \omega_b$ . The propagator in this case is

$$\begin{aligned}U_{2q}(\tau) &= \exp\left(-i\frac{1}{2}\left[\frac{\pi}{4} + \delta\right]\right) [\sigma_x^a \sigma_x^b + \sigma_y^a \sigma_y^b] \\ &- i\frac{\alpha_+}{2} [\sigma_x^a \sigma_x^b - \sigma_y^a \sigma_y^b] \\ &- i\frac{\beta_+ + \beta_-}{2} \sigma_z^a - i\frac{\beta_+ - \beta_-}{2} \sigma_z^b,\end{aligned}\quad (\text{J10})$$

where we have isolated the deviation of  $\alpha_-$  from the ideal value of  $\pi/4$ ,  $\alpha_- = (\pi/4) + \delta$ . We may now read off the Bloch-Siegert shifts  $\omega_{\text{BS},\mu}$ , given by  $\omega_{\text{BS},a} = (\beta_+ + \beta_-)/\tau$  and  $\omega_{\text{BS},b} = (\beta_+ - \beta_-)/\tau$ . With the propagator in hand, we may now compute the gate fidelity using the standard formula [52]

$$F = \frac{\text{Tr}[U^\dagger(\tau)U(\tau)] + \left|\text{Tr}[U_T^\dagger U(\tau)]\right|^2}{d(d+1)},\quad (\text{J11})$$

where  $d$  is the dimension of the Hilbert space and  $U_T$  is the target unitary. Expanding  $\text{Tr}[U_T^\dagger U(\tau)]$  about  $(\delta, \alpha_+, \beta_-, \beta_+) = (0, 0, 0, 0)$  and retaining only leading-order terms, we obtain

$$F = 1 - \frac{2}{5} \left( \alpha_+^2 + \delta^2 + \beta_+^2 + \frac{8}{\pi^2} \beta_-^2 \right),\quad (\text{J12})$$

in the case of  $\sqrt{i\text{SWAP}}$  and

$$F = 1 - \frac{2}{5} \left( \alpha_-^2 + \delta^2 + \beta_-^2 + \frac{8}{\pi^2} \beta_+^2 \right),\quad (\text{J13})$$

in the case of  $\sqrt{b\text{SWAP}}$  (with  $\delta$  now defined as  $\alpha_+ = (\pi/4) + \delta$ ). Evaluating the integrals  $\alpha_\pm, \beta_\pm$  numerically, we obtain  $1 - F = 1.4 \times 10^{-4}$  and  $1.1 \times 10^{-5}$ , in the cases of  $\sqrt{i\text{SWAP}}$  and  $\sqrt{b\text{SWAP}}$ , respectively. For the Bloch-Siegert shifts, we obtain  $|\omega_{\text{BS},a}|/2\pi = 9$  kHz and  $|\omega_{\text{BS},b}|/2\pi = 20$  kHz in the case of  $\sqrt{i\text{SWAP}}$  and  $|\omega_{\text{BS},a}|/2\pi = 11$  kHz and  $|\omega_{\text{BS},b}|/2\pi = 2$  kHz in the case of  $\sqrt{b\text{SWAP}}$ .

We compare the fidelity results with estimates obtained by numerical simulation of Eq. (J3) using QuTiP [53]. These simulations yield infidelity contributions of  $8.4 \times 10^{-5}$  and  $1.3 \times 10^{-5}$  for  $\sqrt{i\text{SWAP}}$  and  $\sqrt{b\text{SWAP}}$ , respectively. In both cases, the analytically estimated values are within about a factor of 2 of the numerically obtained infidelities.

In the case of single-qubit gates with  $U_T = \sqrt{X_\mu}$ , we obtain, for the fidelity to leading order,

$$F = 1 - \frac{4\beta^2}{3\pi^2} - \frac{\delta^2}{6},\quad (\text{J14})$$

where  $\delta = \alpha - (\pi/2)$ . We obtain infidelity estimates of  $7.8 \times 10^{-5}$  and  $7.5 \times 10^{-5}$  for  $\sqrt{X_a}$  and  $\sqrt{X_b}$ , respectively. Performing numerical simulations [with the single-qubit version of Eq. (J3)], we obtain infidelities of  $5.6 \times 10^{-5}$  in both cases. These results are slightly lower than the analytical estimates but of the same order of magnitude.

## 2. Carrier-envelope variations

The phase  $\theta_{\text{CE}}$  is constantly updated during the experiment. As the logical states are defined in the rotating frame, the phase of the pulse should be matched with the dynamical phase difference of the states being swapped. Besides, we make use of the phase  $\theta_{\text{CE}}$  to realize virtual  $Z$  gates. Because the pulse length is only four (11) drive periods in the case of the  $\sqrt{i\text{SWAP}}$  ( $\sqrt{b\text{SWAP}}$ ) gate, the energy carried by the pulse is generally a function of  $\theta_{\text{CE}}$  (to be contrasted with the more standard case in which the pulse length is much larger than the drive period and there is no such dependence on  $\theta_{\text{CE}}$ ). Additionally, the effects of the counter-rotating terms can depend on  $\theta_{\text{CE}}$ . To quantify the contribution of this source of error, we numerically sweep the phase of the pulse and calculate the gate infidelity as a function of  $\theta_{\text{CE}}$ . The average of the increase in infidelity due to phase variation is what is taken as the contribution from carrier-envelope phase in Table II.

TABLE II. The error budget for single- and two-qubit gates. Analytical estimates of decoherence rates can be found in Ref. [48]. We use gate lengths  $\tau = 83.3, 65.1, 101.6$ , and 257.8 ns for the gates  $\sqrt{X_a}$ ,  $\sqrt{X_b}$ ,  $\sqrt{bswap}$ , and  $\sqrt{iswap}$ , respectively. The unaccounted error is attributed to insufficient calibration and rf-flux crosstalk.

Error source	$\sqrt{iSWAP}$	$\sqrt{bswap}$	$\sqrt{X_a}$	$\sqrt{X_b}$
Estimated (Simulated)	Estimated (Simulated)	Estimated (Simulated)	Estimated (Simulated)	Estimated (Simulated)
Decay	$4.6 \times 10^{-4}$ ( $4.6 \times 10^{-4}$ )	$1.8 \times 10^{-4}$ ( $1.8 \times 10^{-4}$ )	$1.5 \times 10^{-4}$ ( $1.5 \times 10^{-4}$ )	$1.1 \times 10^{-4}$ ( $1.2 \times 10^{-4}$ )
Heating	$4.6 \times 10^{-4}$ ( $4.6 \times 10^{-4}$ )	$1.8 \times 10^{-4}$ ( $1.8 \times 10^{-4}$ )	$1.5 \times 10^{-4}$ ( $1.5 \times 10^{-4}$ )	$1.1 \times 10^{-4}$ ( $1.2 \times 10^{-4}$ )
Dephasing	$3.0 \times 10^{-4}$ ( $3.0 \times 10^{-4}$ )	$1.2 \times 10^{-4}$ ( $1.2 \times 10^{-4}$ )	$1.0 \times 10^{-4}$ ( $1.0 \times 10^{-4}$ )	$7.5 \times 10^{-5}$ ( $7.5 \times 10^{-5}$ )
Beyond RWA	$1.4 \times 10^{-4}$ ( $8.4 \times 10^{-5}$ )	$1.1 \times 10^{-5}$ ( $1.3 \times 10^{-5}$ )	$5.2 \times 10^{-5}$ ( $5.6 \times 10^{-5}$ )	$7.5 \times 10^{-5}$ ( $5.6 \times 10^{-5}$ )
Carrier-envelope phase	$(5.8 \times 10^{-5})$ $(8.5 \times 10^{-5})$	$(1.4 \times 10^{-5})$ $(2.3 \times 10^{-5})$	$(0.5 \times 10^{-5})$ $(1.4 \times 10^{-5})$	$(0.5 \times 10^{-5})$ $(2.2 \times 10^{-5})$
Higher-order drive terms	$1.2 \times 10^{-3}$	$4.8 \times 10^{-4}$	$4.0 \times 10^{-4}$	$3.0 \times 10^{-4}$
Estimated infidelity (decoherence)	$1.4 \times 10^{-3}$	$5.3 \times 10^{-4}$	$4.7 \times 10^{-4}$	$3.7 \times 10^{-4}$
Simulated infidelity (all)	$2.8 \times 10^{-3}$	$9 \times 10^{-4}$	$6 \times 10^{-4}$	$5 \times 10^{-4}$
Measured infidelity				

### 3. Higher-order drive terms

As discussed in Ref. [27], the form of the drive operator in Eq. (J1) is an approximation. In reality, the drive operator associated with  $\Phi_{\text{ext},C}$  is not perfectly  $XX$  but includes also nonzero  $IX$ ,  $XI$ , and other components. Similarly, for the drive operators associated with  $\Phi_{\text{ext},A}$  and  $\Phi_{\text{ext},B}$ , the drive operators contain nonzero  $ZX$ ,  $XZ$ , and other terms. Including these additional drive terms in the simulations contributes infidelities on the order of  $10^{-5}$  (see Table II).

### 4. Decoherence

The gate fidelity is reduced due to decay, heating, and dephasing effects. In the following, we specialize to the case of the  $\sqrt{iSWAP}$  gate, taking  $\omega_d = |\omega_b - \omega_a|$ . The discussion follows similarly for the case of  $\sqrt{bswap}$ , with  $\omega_d = \omega_b + \omega_a$ . The Hamiltonian after performing the RWA is

$$H'_{\text{RWA}} = \frac{A}{4}(\sigma_x^A \sigma_x^B + \sigma_y^A \sigma_y^B). \quad (\text{J15})$$

We perform numerical simulations of the Lindblad master equation

$$\frac{d\rho(t)}{dt} = -i[H'_{\text{RWA}}, \rho(t)] + \sum_k \Gamma_k \mathcal{D}(L_k) \rho(t), \quad (\text{J16})$$

where

$$\mathcal{D}(L)\rho = L\rho L^\dagger - \frac{1}{2}\{L^\dagger L, \rho\}$$

is the dissipator and  $\rho(t)$  is the system density matrix. We include collapse operators  $\sigma_-^\mu$ ,  $\sigma_+^\mu$ , and  $\sigma_z^\mu$  and associated decay rates  $\Gamma_1/2$ ,  $\Gamma_1/2$ , and  $\Gamma_\phi/2$ , respectively ( $\mu = \{A, B\}$ ). The factors of  $1/2$  in the decay and heating rates are due to the equal contributions of decay and heating to  $T_1$ , while the factor of  $1/2$  in the dephasing rate ensures that coherences decay at the appropriate rate [48]. By turning on each decoherence channel one at a time, we numerically estimate the contribution of each (see Table II). We then proceed to turn on all decoherence channels to estimate the overall fidelity reduction due to decoherence. For both the  $\sqrt{bswap}$  and  $\sqrt{iSWAP}$  gates, decoherence makes up about half of the measured infidelity.

Analytical estimates of the first-order contribution of decoherence to the infidelity are given in Ref. [48] and we reproduce them here for completeness:

$$F \approx 1 - \frac{d}{2(d+1)}\tau \sum_\mu (\Gamma_1^\mu + \Gamma_\phi^\mu), \quad (\text{J17})$$

where  $\tau$  is the duration of the gate and  $d$  is the dimension of the Hilbert space. Infidelity estimates using this formula for single- and two-qubit gates can be found in Table II. We find excellent agreement between the numerical results and analytical formulas.

## 5. The rf-flux crosstalk

As discussed in Appendix D, flux crosstalk can contribute to dynamic frequency shifts and unwanted entanglement. Defining the maximum fluxes due to crosstalk  $\xi_\mu$  through the qubit loops, the qubit drive amplitudes are  $\Omega_{ct,\mu} = \xi_\mu E_{L\mu} \langle 0 | \phi_\mu | 1 \rangle$ , where  $\mu = a, b$ . To estimate the infidelity associated with such crosstalk, we substitute Eq. (D1) for Eq. (J1), including the Gaussian envelope and transforming into the rotating frame with the qubit frequencies. For  $\xi_\mu/2\pi = 10^{-4}$ , we find numerically that the infidelity is  $1.2 \times 10^{-6}$  and  $1.2 \times 10^{-5}$  for  $\sqrt{bSWAP}$  and  $\sqrt{iSWAP}$ , respectively, below the levels to which we are sensitive. However, if crosstalk rises to the level of  $\xi_\mu/2\pi = 10^{-3}$ , the infidelities rise to  $1.1 \times 10^{-3}$  and 0.069 for  $\sqrt{bSWAP}$  and  $\sqrt{iSWAP}$ , respectively. These infidelities would be the leading source of error, necessitating the careful flux-crosstalk cancellation that we undertake in our experiment.

## 6. Overall error budget

With all of the error channels included, the infidelities of the single-qubit,  $\sqrt{iSWAP}$ , and  $\sqrt{bSWAP}$  gates are reduced to 99.97%, 99.87%, and 99.95%, respectively. Our numerical simulations suggest that the gate fidelity is predominantly constrained by decoherence. The remaining error is attributed to insufficient calibration and rf-flux crosstalk.

- 
- [1] F. Arute, K. Arya, R. Babbush, D. Bacon, J. C. Bardin, R. Barends, R. Biswas, S. Boixo, F. G. Brandao, and D. A. Buell, *et al.*, Quantum supremacy using a programmable superconducting processor, *Nature* **574**, 505 (2019).
- [2] Y. Kim, A. Eddins, S. Anand, K. X. Wei, E. Van Den Berg, S. Rosenblatt, H. Nayfeh, Y. Wu, M. Zaletel, and K. Temme, *et al.*, Evidence for the utility of quantum computing before fault tolerance, *Nature* **618**, 500 (2023).
- [3] M. H. Devoret and R. J. Schoelkopf, Superconducting circuits for quantum information: An outlook, *Science* **339**, 1169 (2013).
- [4] P. Krantz, M. Kjaergaard, F. Yan, T. P. Orlando, S. Gustavsson, and W. D. Oliver, A quantum engineer's guide to superconducting qubits, *Appl. Phys. Rev.* **6**, 021318 (2019).
- [5] V. Sivak, A. Eickbusch, B. Royer, S. Singh, I. Tsoutsios, S. Ganjam, A. Miano, B. Brock, A. Ding, and L. Frunzio, *et al.*, Real-time quantum error correction beyond break-even, *Nature* **616**, 50 (2023).
- [6] J. Koch, T. M. Yu, J. Gambetta, A. A. Houck, D. I. Schuster, J. Majer, A. Blais, M. H. Devoret, S. M. Girvin, and R. J. Schoelkopf, Charge-insensitive qubit design derived from the Cooper pair box, *Phys. Rev. A* **76**, 042319 (2007).
- [7] A. P. Place, L. V. Rodgers, P. Mundada, B. M. Smitham, M. Fitzpatrick, Z. Leng, A. Premkumar, J. Bryon, A. Vrajitoarea, and S. Sussman, *et al.*, New material platform for superconducting transmon qubits with coherence times exceeding 0.3 milliseconds, *Nat. Commun.* **12**, 1779 (2021).
- [8] A. G. Fowler, M. Mariantoni, J. M. Martinis, and A. N. Cleland, Surface codes: Towards practical large-scale quantum computation, *Phys. Rev. A* **86**, 032324 (2012).
- [9] Y. Sung, L. Ding, J. Braumüller, A. Vepsäläinen, B. Kannan, M. Kjaergaard, A. Greene, G. O. Samach, C. McNally, and D. Kim, *et al.*, Realization of high-fidelity CZ and ZZ-free iSWAP gates with a tunable coupler, *Phys. Rev. X* **11**, 021058 (2021).
- [10] V. Negîrneac, H. Ali, N. Muthusubramanian, F. Battistel, R. Sagastizabal, M. S. Moreira, J. F. Marques, W. J. Vlothuizen, M. Beekman, C. Zachariadis, N. Haider, A. Bruno, and L. DiCarlo, High-fidelity controlled-Z gate with maximal intermediate leakage operating at the speed limit in a superconducting quantum processor, *Phys. Rev. Lett.* **126**, 220502 (2021).
- [11] V. E. Manucharyan, J. Koch, L. I. Glazman, and M. H. Devoret, Fluxonium: Single Cooper-pair circuit free of charge offsets, *Science* **326**, 113 (2009).
- [12] H. Zhang, S. Chakram, T. Roy, N. Earnest, Y. Lu, Z. Huang, D. K. Weiss, J. Koch, and D. I. Schuster, Universal fast-flux control of a coherent, low-frequency qubit, *Phys. Rev. X* **11**, 011010 (2021).
- [13] N. Earnest, S. Chakram, Y. Lu, N. Irons, R. K. Naik, N. Leung, L. Ocola, D. A. Czaplewski, B. Baker, J. Lawrence, J. Koch, and D. I. Schuster, Realization of a  $\Lambda$  system with metastable states of a capacitively shunted fluxonium, *Phys. Rev. Lett.* **120**, 150504 (2018).
- [14] Y.-H. Lin, L. B. Nguyen, N. Grabon, J. San Miguel, N. Pankratova, and V. E. Manucharyan, Demonstration of protection of a superconducting qubit from energy decay, *Phys. Rev. Lett.* **120**, 150503 (2018).
- [15] L. B. Nguyen, Y.-H. Lin, A. Somoroff, R. Mencia, N. Grabon, and V. E. Manucharyan, High-coherence fluxonium qubit, *Phys. Rev. X* **9**, 041041 (2019).
- [16] A. Somoroff, Q. Ficheux, Raymond A. Mencia, H. Xiong, R. Kuzmin, and Vladimir E. Manucharyan, Millisecond coherence in a superconducting qubit, *Phys. Rev. Lett.* **130**, 267001 (2023).
- [17] L. Ding, M. Hays, Y. Sung, B. Kannan, J. An, A. Di Paolo, A. H. Karamlou, T. M. Hazard, K. Azar, D. K. Kim, B. M. Niedzielski, A. Melville, M. E. Schwartz, J. L. Yoder, T. P. Orlando, S. Gustavsson, J. A. Grover, K. Serniak, and W. D. Oliver, High-fidelity, frequency-flexible two-qubit fluxonium gates with a transmon coupler, *Phys. Rev. X* **13**, 031035 (2023).
- [18] Q. Ficheux, L. B. Nguyen, A. Somoroff, H. Xiong, K. N. Nesterov, M. G. Vavilov, and V. E. Manucharyan, Fast logic with slow qubits: Microwave-activated controlled-Z gate on low-frequency fluxoniums, *Phys. Rev. X* **11**, 021026 (2021).
- [19] E. Dogan, D. Rosenstock, L. Le Guevel, H. Xiong, R. A. Mencia, A. Somoroff, K. N. Nesterov, M. G. Vavilov, V. E. Manucharyan, and C. Wang, Two-fluxonium cross-resonance gate, *Phys. Rev. Appl.* **20**, 024011 (2023).
- [20] F. Bao, H. Deng, D. Ding, R. Gao, X. Gao, C. Huang, X. Jiang, H.-S. Ku, Z. Li, and X. Ma, *et al.*, Fluxonium: An alternative qubit platform for high-fidelity operations, *Phys. Rev. Lett.* **129**, 010502 (2022).

- [21] H. Xiong, Q. Ficheux, A. Somoroff, L. B. Nguyen, E. Dogan, D. Rosenstock, C. Wang, K. N. Nesterov, M. G. Vavilov, and V. E. Manucharyan, Arbitrary controlled-phase gate on fluxonium qubits using differential ac Stark shifts, *Phys. Rev. Res.* **4**, 023040 (2022).
- [22] I. N. Moskalenko, I. A. Simakov, N. N. Abramov, A. A. Grigorev, D. O. Moskalev, A. A. Pishchimova, N. S. Smirnov, E. V. Zikiy, I. A. Rodionov, and I. S. Besedin, High fidelity two-qubit gates on fluxonions using a tunable coupler, *npj Quantum Inf.* **8**, 130 (2022).
- [23] Y. Chen, C. Neill, P. Roushan, N. Leung, M. Fang, R. Barends, J. Kelly, B. Campbell, Z. Chen, and B. Chiaro, *et al.*, Qubit architecture with high coherence and fast tunable coupling, *Phys. Rev. Lett.* **113**, 220502 (2014).
- [24] M. R. Geller, E. Donate, Y. Chen, M. T. Fang, N. Leung, C. Neill, P. Roushan, and J. M. Martinis, Tunable coupler for superconducting Xmon qubits: Perturbative nonlinear model, *Phys. Rev. A* **92**, 012320 (2015).
- [25] S. H. W. van der Ploeg, A. Izmalkov, A. M. van den Brink, U. Hübner, M. Grajcar, E. Il'ichev, H.-G. Meyer, and A. M. Zagoskin, Controllable coupling of superconducting flux qubits, *Phys. Rev. Lett.* **98**, 057004 (2007).
- [26] A. O. Niskanen, K. Harrabi, F. Yoshihara, Y. Nakamura, S. Lloyd, and J. S. Tsai, Quantum coherent tunable coupling of superconducting qubits, *Science* **316**, 723 (2007).
- [27] D. K. Weiss, H. Zhang, C. Ding, Y. Ma, D. I. Schuster, and J. Koch, Fast high-fidelity gates for galvanically-coupled fluxonium qubits using strong flux modulation, *PRX Quantum* **3**, 040336 (2022).
- [28] C. Wang, X. Li, H. Xu, Z. Li, J. Wang, Z. Yang, Z. Mi, X. Liang, T. Su, and C. Yang, *et al.*, Towards practical quantum computers: Transmon qubit with a lifetime approaching 0.5 milliseconds, *npj Quantum Inf.* **8**, 3 (2022).
- [29] G. Dolan, Offset masks for lift-off photoprocessing, *Appl. Phys. Lett.* **31**, 337 (1977).
- [30] D. Ristè, J. G. van Leeuwen, H.-S. Ku, K. W. Lehnert, and L. DiCarlo, Initialization by measurement of a superconducting quantum bit circuit, *Phys. Rev. Lett.* **109**, 050507 (2012).
- [31] R. Gebauer, N. Karcher, D. Gusekova, M. Spiecker, L. Grünhaupt, I. Takmakov, P. Winkel, L. Planat, N. Roch, and W. Wernsdorfer, *et al.*, in *Fifth International Conference on Quantum Technologies (ICQT-2019), 15–19 July 2019, Moscow, Russia*, Vol. 2241 (AIP Publishing, 2020).
- [32] L. Stefanazzi, K. Treptow, N. Wilcer, C. Stoughton, C. Bradford, S. Uemura, S. Zorzetti, S. Montella, G. Cancelo, and S. Sussman, *et al.*, The QICK (Quantum Instrumentation Control Kit): Readout and control for qubits and detectors, *Rev. Sci. Inst.* **93**, 044709 (2022).
- [33] A. Somoroff, P. Truitt, A. Weis, J. Bernhardt, D. Yohannes, J. Walter, K. Kalashnikov, M. Renzullo, R. A. Mencia, M. G. Vavilov, V. E. Manucharyan, I. V. Vernik, and O. A. Mukhanov, Fluxonium qubits in a flip-chip package, *Phys. Rev. Appl.* **21**, 024015 (2024).
- [34] X. Dai, D. Tennant, R. Trappen, A. Martinez, D. Melanson, M. Yurtalan, Y. Tang, S. Novikov, J. Grover, S. Disseler, J. Basham, R. Das, D. Kim, A. Melville, B. Niedzielski, S. Weber, J. Yoder, D. Lidar, and A. Lupascu, Calibration of flux crosstalk in large-scale flux-tunable superconducting quantum circuits, *PRX Quantum* **2**, 040313 (2021).
- [35] A. Dunsworth, R. Barends, Y. Chen, Z. Chen, B. Chiaro, A. Fowler, B. Foxen, E. Jeffrey, J. Kelly, and P. Klimov, *et al.*, A method for building low loss multi-layer wiring for superconducting microwave devices, *Appl. Phys. Lett.* **112**, 00 (2018).
- [36] D. C. McKay, C. J. Wood, S. Sheldon, J. M. Chow, and J. M. Gambetta, Efficient Z gates for quantum computing, *Phys. Rev. A* **96**, 022330 (2017).
- [37] J. M. Chow, J. M. Gambetta, L. Tornberg, J. Koch, L. S. Bishop, A. A. Houck, B. R. Johnson, L. Frunzio, S. M. Girvin, and R. J. Schoelkopf, Randomized benchmarking and process tomography for gate errors in a solid-state qubit, *Phys. Rev. Lett.* **102**, 090502 (2009).
- [38] J. M. Gambetta, F. Motzoi, S. T. Merkel, and F. K. Wilhelm, Analytic control methods for high-fidelity unitary operations in a weakly nonlinear oscillator, *Phys. Rev. A* **83**, 012308 (2011).
- [39] C. Neill, *et al.*, A blueprint for demonstrating quantum supremacy with superconducting qubits, *Science* **360**, 195 (2018).
- [40] S. T. Merkel, J. M. Gambetta, J. A. Smolin, S. Poletto, A. D. Córcoles, B. R. Johnson, C. A. Ryan, and M. Steffen, Self-consistent quantum process tomography, *Phys. Rev. A* **87**, 062119 (2013).
- [41] S. Boixo, S. V. Isakov, V. N. Smelyanskiy, R. Babbush, N. Ding, Z. Jiang, M. J. Bremner, J. M. Martinis, and H. Neven, Characterizing quantum supremacy in near-term devices, *Nat. Phys.* **14**, 595 (2018).
- [42] E. Magesan, J. M. Gambetta, B. R. Johnson, C. A. Ryan, J. M. Chow, S. T. Merkel, M. P. da Silva, G. A. Keefe, M. B. Rothwell, T. A. Ohki, M. B. Ketchen, and M. Steffen, Efficient measurement of quantum gate error by interleaved randomized benchmarking, *Phys. Rev. Lett.* **109**, 080505 (2012).
- [43] P. Groszkowski and J. Koch, SCQUBITS: A PYTHON package for superconducting qubits, *Quantum* **5**, 583 (2021).
- [44] S. P. Chitta, T. Zhao, Z. Huang, I. Mondragon-Shem, and J. Koch, Computer-aided quantization and numerical analysis of superconducting circuits, *New J. Phys.* **24**, 103020 (2022).
- [45] G. Zhu, D. G. Ferguson, V. E. Manucharyan, and J. Koch, Circuit QED with fluxonium qubits: Theory of the dispersive regime, *Phys. Rev. B* **87**, 024510 (2013).
- [46] A. Blais, J. Gambetta, A. Wallraff, D. I. Schuster, S. M. Girvin, M. H. Devoret, and R. J. Schoelkopf, Quantum-information processing with circuit quantum electrodynamics, *Phys. Rev. A* **75**, 032329 (2007).
- [47] M. Ganzhorn, G. Salis, D. J. Egger, A. Fuhrer, M. Mergenthaler, C. Müller, P. Müller, S. Paredes, M. Pechal, and M. Werninghaus, *et al.*, Benchmarking the noise sensitivity of different parametric two-qubit gates in a single superconducting quantum computing platform, *Phys. Rev. Res.* **2**, 033447 (2020).
- [48] T. Abad, J. Fernández-Pendás, A. Frisk Kockum, and G. Johansson, Universal fidelity reduction of quantum operations from weak dissipation, *Phys. Rev. Lett.* **129**, 150504 (2022).
- [49] R. M. Wilcox, Exponential operators and parameter differentiation in quantum physics, *J. Math. Phys.* **8**, 962 (1967).

- [50] S. Blanes, F. Casas, J. A. Oteo, and J. Ros, The Magnus expansion and some of its applications, *Phys. Rep.* **470**, 151 (2009).
- [51] W. Magnus, On the exponential solution of differential equations for a linear operator, *Commun. Pure Appl. Math.* **7**, 649 (1954).
- [52] L. H. Pedersen, N. M. Møller, and K. Mølmer, Fidelity of quantum operations, *Phys. Lett. A* **367**, 47 (2007).
- [53] J. Johansson, P. Nation, and F. Nori, QuTiP 2: A PYTHON framework for the dynamics of open quantum systems, *Comput. Phys. Commun.* **184**, 1234 (2013).